# The ECHOWAVE Hindcast

## A 30-years high resolution database for wave energy applications in North Atlantic European waters

Alday, Matías; Lavidas, George

**DOI**
10.1016/j.renene.2024.121391

**Publication date**
2024

**Document Version**
Final published version

**Published in**
Renewable Energy

**Citation (APA)**
Alday, M., & Lavidas, G. (2024). The ECHOWAVE Hindcast: A 30-years high resolution database for wave energy applications in North Atlantic European waters. *Renewable Energy*, *236*, Article 121391. https://doi.org/10.1016/j.renene.2024.121391

Renewable Energy 236 (2024) 121391

Contents lists available at ScienceDirect

Renewable Energy

journal homepage: www.elsevier.com/locate/renene

# The ECHOWAVE Hindcast: A 30-years high resolution database for wave energy applications in North Atlantic European waters

Matías Alday *, George Lavidas

*Marine Renewable Energies Lab., Offshore Engineering group, Department of Hydraulic Engineering, Delft University of Technology, Stevinweg 1, Delft, 2628 CN, The Netherlands*

## ARTICLE INFO

Dataset link: https://www.tudelft.nl/ceg/mrel

*Keywords:*
Hindcast
Wave energy
North Atlantic
WAVEWATCH III

## ABSTRACT

The ECHOWAVE hindcast is an open source dataset specially developed for wave climate and energy applications within European Atlantic waters. It provides high resolution (∼ 2.3 km) fields of wave parameters and spectral data allowing for a detailed characterization of the wave resource within the coastal shelf. This is of importance for depths < 200 m, where most deployment projects of wave energy converters (WEC) take place. Model setup and adjustments, leading to parameterization TUD-165, were specially aimed to improve the sea states' characterization within the North-East Atlantic. The effects on accuracy of these adjustments and extensive validation, were done mainly comparing simulations with significant wave heights ($H_s$) from the European Space Agency CCI Version 3 altimeter dataset. Verification of other wave parameters and the spectral energy comparing with in situ measurements were also included. Results show that TUD-165 helps to reduce about 5% the $H_s$ bias of the most frequent waves compared to T475 proposed by Alday et al. (2021), and an overall better performance than ERA5 within the North-East Atlantic. Compared to WAVERYS, ECHOWAVE performs better for $H_s > 9.5$ m, with constrained bias between −2 to 5%. The accurate estimation of "extreme" waves is important to avoid WECs survivability over-estimations.

## 1. Introduction

In recent years, we have experienced a significant interest for the utilization of renewable resources in the marine environment. The wave resource represents one of the most interesting alternatives given its abundance, and the large amount of potential sites for energy extraction worldwide [1,2]. As a result, the number of studies dedicated to quantify the available wave resource have increased throughout the years (e.g.; [3–8]). A prime example of the opportunities and efforts put into the energy transition, is the Offshore Energy Strategy of the European Commission. It sets a clear target of at least 40 GW of marine energies by 2050 [9].

In the last decade, there has been a vast amount of large wave datasets (hindcasts/reanalyses) made available to the public for several applications, e.g.: [10–17]. These databases have been created with different objectives in mind and using particular model setups, including different forcing fields, physical parameterizations, and numerical choices. In some cases, data assimilation is also included, as done in the reanalyses described in [13,18]. The use of these wave products have been key to progressively improve our understanding of the sea states. Nevertheless, it is expected to find differences between them [19,20], with different levels of accuracy for particular regions and/or consistency in time [21].

One of the main sources of uncertainty in the estimation of the available wave power is typically related to the accuracy of the used data. This is specially true when the analysis is based on models' output [22]. For open ocean applications, wave models like WAM [23] or WAVEWATCH III [24,25] can have an errors in the estimation of the significant wave height ($H_s$) of about 10% or smaller. The continuous improvement of spectral models to extend their applications to coastal zones, have allowed to reach similar accuracy levels in zones with intermediate to shallow waters [26].

In the present paper, the implementation and validation of the ECHOWAVE hindcast for European waters in the North Atlantic is presented. ECHOWAVE is the acronym used for **E**uropean **CO**asts **H**igh Resolution **O**cean **WAVE**s Hindcast. The dataset was developed using WAVEWATCH III (from hereon WW3) employing a 2-way nesting multi-grid scheme [27] to progressively increase spatial resolution closer to the coast (to about 2.3 km). The hindcast generation was designed specially to provide reliable sea states' characterization for wave energy applications. Primarily, to reduce uncertainties in the wave resource estimation within European coastal waters. In this sense,

---

* Corresponding author.
*E-mail addresses:* M.F.AldayGonzalez@tudelft.nl (M. Alday), G.Lavidas@tudelft.nl (G. Lavidas).

https://doi.org/10.1016/j.renene.2024.121391
Received 2 May 2024; Received in revised form 7 August 2024; Accepted 16 September 2024

there are 3 main characteristics from this dataset to highlight. First, all physical parameterizations adjustments are applied to improve the performance within the North-East Atlantic. This approach allowed to reduce the bias for a wide range of wave heights in the area of interest (compared to existing datasets). Second, adjustments' verification and extensive validation is done using the latest ESA Sea State CCI V3 altimeter dataset [28], which is adequate for coastal applications [26,29,30]. Third, its regular high resolution within coastal areas, for depths $\leq$ 200 m, allows for a detailed characterization of the wave resource, and more accurate coupling of WECs [31].

The study presents a detailed calibration/validation for this new database (ECHOWAVE) that aims to offer new high-fidelity metocean information for the whole European Atlantic coastlines. This work also evaluates the accuracy of coarser databases and underlines their pitfalls in the nearshore, where the sea states are better resolved by ECHOWAVE thanks to the adjusted physical parameterizations and resolution.

The content of this paper is organized as follows. Method description in Section 2, including wave data sources and expressions used in the analysis. Then, details on the model implementation are included in Section 3. Finally, results and discussion are presented in Section 4 followed by conclusions in Section 6.

## 2. Method

A brief description of the wave data sources and expressions used to assess the model performance are presented in this section.

### 2.1. Wave data

Two main data sources are employed to compare with the model results: Satellite altimeter and in situ buoy data.

The European Space Agency Climate Change Initiative (CCI) V3 altimeter product [28] is mainly used to estimate the model results' accuracy at basin scales. The significant wave height (SWH) "denoised" variable at 1 Hz (with ∼ 7 km along-track resolution) is employed to compare with modeled $H_s$. Given its suitability for coastal applications, the CCI V3 altimeter data is also used to analyze the performance of the simulated $H_s$ within the European coastal shelf.

Buoy data was obtained from the CMEMS In Situ Thematic Assembly Center (TAC). Time series of $H_s$, $T_p$ (peak period) and $T_{02}$ (mean period) were used to compare with model results at specific locations. The selected buoys used in this study are specified in Table 1. Their locations can also be seen in Fig. B.14 (Appendix B).

Additionally, the WAVERYS and the well known ERA5 wave product are included to compare their performance with the ECHOWAVE hindcast (see Section 4.4). WAVERYS is a global reanalysis that presents 3-hourly wave parameters' fields with a spatial resolution of 0.2°. This dataset was created using ERA5 winds and sea ice, and the GLORYS12 ocean currents [32] as forcing fields. It assimilates altimeter data from different past missions (from ERS1, Topex-Poseidon until Sentinel-3 A). Wave spectra from synthetic aperture radar (SAR) given by Sentinel-1 A and 1B is also assimilated in WAVERYS to improve the simulation of swell propagation [18].

### 2.2. Performance analysis

The following skill parameters are used to assess the accuracy of the modeled sea states: The normalized mean bias (NMB), scatter index (SI), and the Hanna and Heinold index (HH).

$$\mathrm{NMB}(X) = \frac{\sum (X_{\mathrm{mod}} - X_{\mathrm{obs}})}{\sum X_{\mathrm{obs}}} \tag{1}$$

$$\mathrm{SI}(X) = \sqrt{\frac{\sum \left[ (X_{\mathrm{mod}} - \overline{X_{\mathrm{mod}}}) - (X_{\mathrm{obs}} - \overline{X_{\mathrm{obs}}}) \right]^2}{\sum X_{\mathrm{obs}}^2}} \tag{2}$$

**Table 1**
Selected buoys for validation.

| Buoy ID | Longitude | Latitude | Data type |
|---|---|---|---|
| 6200001 | 4.994° | 45.222° | Spectral |
| 6200024 | 3.040° | 43.640° | Wave parameters |
| 6200025 | −6.167° | 43.733° | Wave parameters |
| 6200027 | −2.218° | 49.082° | Wave parameters |
| 6200029 | −12.401° | 48.701° | Wave parameters |
| 6200066 | −1.614° | 43.530° | Spectral |
| 6200069 | −4.968° | 48.290° | Spectral/Wave param. |
| 6200080 | −1.833° | 45.916° | Spectral |
| 6200081 | −13.301° | 51.00° | Wave parameters |
| 6200082 | −7.618° | 44.064° | Wave parameters |
| 6200083 | −9.21° | 43.490° | Wave parameters |
| 6200084 | −9.374° | 42.121° | Wave parameters |
| 6200091 | −5.431° | 53.484° | Wave parameters |
| 6200093 | −9.999° | 55.002° | Wave parameters |
| 6200095 | −15.862° | 53.017° | Wave parameters |
| 6200103 | −2.900° | 49.900° | Wave parameters |
| 6200105 | −12.367° | 54.550° | Wave parameters |
| 6200144 | 1.70° | 53.40° | Wave parameters |
| 6200191 | −9.580° | 41.150° | Wave parameters |
| 6200192 | −9.640° | 39.510° | Wave parameters |
| 6200199 | −9.210° | 39.560° | Wave parameters |
| 6200301 | −4.50° | 52.30° | Wave parameters |
| 6200303 | −5.100° | 51.603° | Wave parameters |
| 6300110 | 1.50° | 59.50° | Wave parameters |
| 6300112 | 1.00° | 61.10° | Wave parameters |
| 6400045 | −11.401° | 59.100° | Wave parameters |
| 6400046 | −4.500° | 60.701° | Wave parameters |
| A121 | 3.817° | 55.417° | Wave parameters |
| D151 | 2.933° | 54.317° | Wave parameters |
| Donostia-buoy | −2.026° | 43.569° | Wave parameters |
| Ekofisk | 3.224° | 56.543° | Wave parameters |
| F161 | 4.017° | 54.117° | Wave parameters |
| J61 | 2.950° | 53.817° | Wave parameters |
| L91 | 4.961° | 53.614° | Wave parameters |
| NsbIII | 6.783° | 54.683° | Wave parameters |
| Westhinder | 2.436° | 51.381° | Wave parameters |

$$\mathrm{HH}(X) = \sqrt{\frac{\sum (X_{\mathrm{mod}} - X_{\mathrm{obs}})^2}{\sum X_{\mathrm{mod}} X_{\mathrm{obs}}}} \tag{3}$$

In Eq. (1) to Eq. (3) $X_{\mathrm{mod}}$ corresponds to the modeled data (e.g.; $H_s$ or $T_p$) and $X_{\mathrm{obs}}$ is the data from observations, satellite or buoys. $\overline{X}_{\mathrm{mod}}$ and $\overline{X}_{\mathrm{obs}}$ correspond to the mean of the analyzed variable. In particular, when altimeter data is used as a reference to compare with the model output, the NMB, SI and HH are computed from an along-track type analysis. In other words, the closest 4 points from the model field output to an altimeter measurement, are interpolated in time and space to collocate the model data along the satellite track. Also, when performing model adjustments based on comparisons with altimeter data, attention is paid to $H_s \geq 1.0$ m. Accuracy of the altimeters for resolving smaller wave heights typically decreases due to bandwidth limitations [33].

As suggested in [34], the symmetrically normalized root mean squared error HH is included since it is less sensitive to the presence of large biases or fluctuations.

When Eq. (1) is used to compare data from 2 different numerical models, it is then called normalized mean differences (NMD).

### 2.3. Wave energy flux

A generalized expression, considering the effects of intermediate and shallow water depths, is employed to estimate the wave energy flux (pWave). Using the dispersion relation from the linear wave theory [35,36], the wave length ($L$) changes as a function of the local depth is:

$$L = \frac{g}{2\pi} T^2 \tanh(kd) \tag{4}$$

where $g$ is the acceleration of gravity (9.81 $\mathrm{m/s^2}$), $T$ the wave period in s, $d$ is the local depth in m, and $k = 2\pi/L$ is the wave number.

The wave energy flux (or wave power density) is expressed as follows:

$$F_W = \mathrm{pWave} = C_g \frac{1}{16} \rho_w g H^2 \tag{5}$$

with $\rho_w$ the sea water density, here taken as 1026 $\mathrm{kg/m^3}$, and $C_g$ is the wave group celerity given by Eq. (6).

$$C_g = 0.5 \left( 1 + \frac{2kd}{\sinh(2kd)} \right) \tag{6}$$

Combining Eqs. (4) to (6), the expression for the wave energy flux can be written as:

$$\mathrm{pWave} = 0.5 \left( 1 + \frac{2kd}{\sinh(2kd)} \right) \frac{g}{2\pi} T \tanh(kd) \frac{1}{16} \rho_w g H^2 \tag{7}$$

For pWave estimations using spectral wave data, $T$ is replaced by the energy period $T_e$ and $H$ by the significant wave height $H_s$. Here, the wave energy period is estimated as $0.9T_p$ [5]. Although this is a reasonable and widely accepted estimation of the energy period, it must be noted that the conversion factor between $T_p$ and $T_e$ depends on regional wave characteristics [1].

## 3. Model implementation

### 3.1. Domain and nesting scheme

The WW3 implementation includes a multi-grid system with a 2-way nesting scheme, which means that higher rank grids, in this case with higher resolution too, feed spectral information back to the lower rank grids [27,37].

Three regular grids were defined with increasing resolution: The base “coarse” grid N_ATL-15M with a spatial resolution of 0.25°, an intermediate grid for European waters (N_ATL-8M) with 0.125° resolution, and a coastal grid (EU_ATL-2M) with high spatial resolution of 0.03°, Fig. 1 displays the multi-grid nesting scheme layout. N_ATL-15M covers the full North Atlantic basin from latitude 0.25° to 80° North and provides boundary conditions to N_ATL-8M on deep waters, mostly outside the European coastal shelf (see Fig. 1.b). At the same time, N_ATL-8M provides boundary conditions to the coastal grid EU_ATL-2M with active computing nodes only in intermediate to shallow waters. Note that boundary conditions in N_ATL-8M and EU_ATL-2M are prescribed along the outer edge of the active nodes.

### 3.2. Physical parameterizations and numerical choices

Atmosphere–wave interactions are incorporated with the WW3 ST4 parameterizations package [39]. This includes wind-wave growth by Janssen [40] (with modifications from [41,42]), swell attenuation due to the air–sea friction effect [43] and wave breaking. These expressions are described in [39] and [44], with further adjustments proposed in [11].

The 4-waves nonlinear interactions are represented with the Discrete Interaction Approximation (DIA [45]) to reduce computing time. Although this is a rather “simplified” representation, it still allows to capture the main features of the spectrum, namely $H_s$, $T_p$ and $D_p$, which are important for the applications of the generated dataset. Recently, efforts have been made to include the Gaussian Quadrature Method (GQM; [46]) in WW3 to compute the full nonlinear interactions [47]. The GQM have proved to be more efficient compared, for example, to the Webb–Resio–Tracy method (WRT; [48,49]) as implemented by van Vledder [50]. Nevertheless, the GQM implementation is currently adjusted for deep waters applications, and its use with 36 spectral directions (as used here) is still considerably more expensive than the DIA.

The effects of wave scattering in sea ice and potential wave induced ice break-up are included using the IS2 parameterization by Boutin et al. [51] further adjusted by Ardhuin et al. [52]. The effects of wave dissipation below ice plates as function of the boundary layer Reynolds number are also included (IC2; [53]).

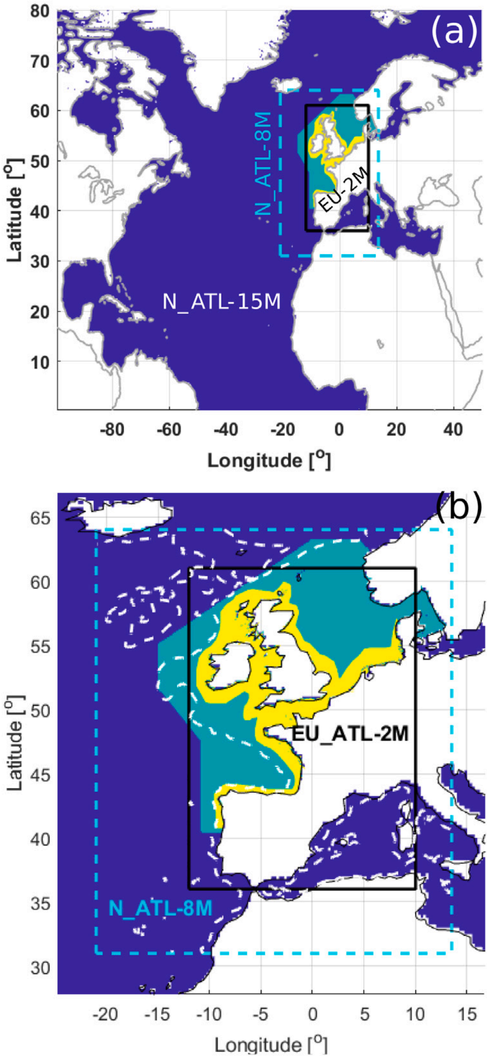

**Fig. 1.** Multi-grid setup for WW3 implementation. (a) Nesting scheme (adapted from [38]). (b) Detail on N_ATL-8M and EU_ATL-2M. Active grid nodes from N_ATL-15M in dark blue. In green active nodes from N_ATL-8M grid. In yellow active nodes from EU_ATL-2M (high resolution grid). Dashed white lines in (b) show the 1000 m depth contours.

Bottom friction effects, more important in intermediate to shallow water depths, are accounted with the SHOWEX parameterization (WW3 switch BT4). This also includes a sub-grid parameterization to account for the variability of water depth [54,55]. We note that the default values suggested in the WW3 user manual [24] are considered for the complete modeled domain. Alternatively, it is possible to prescribe a detailed map of the bottom sediment representative diameter ($D_{50}$) as done in [26] with an unstructured mesh.

Finally, an ad hoc constant 5% reflection is considered at coastlines, using the parameterization described in [56].

Regarding numerical schemes, the Upwind Quickest scheme (UQ; [57,58]) is employed for spatial and spectral advection. The Garden Sprinckler Effect correction is included using the method proposed by Tolman [59]. For all grids, a 36 exponentially spaced frequencies from 0.034 to 0.95 Hz, with an increment factor from one frequency to the next of 1.1. In terms of directional discretization of the spectrum, 24 directions are considered for N_ATL-15M (15° resolution), and 36 directions for N_ATL-8M and EU_ATL-2M (10° resolution).

Output frequency for wave parameters' fields and wave spectrum time series (at specific locations) is 1 h.

### 3.3. Adjusted expressions

As shown in Section 4.1, a particular set of parameters are adjusted from the atmosphere–wave interactions parameterization. Changes are introduced mainly in parameters from the wind-wave growth and swell dissipation expressions. These adjustments are aimed to improve the spectral growth-dissipation balance which in the end helps to reduce overall $H_s$ bias and improve wave heights' distribution. Here, a brief description is provided only for the expressions where terms are modified. For further details on this set of parameterizations refer to Ardhuin et al. [39] and The WAVEWATCH III® Development Group [24].

The atmosphere–wave interactions source term as defined in [39] has the following form:

$$S_{\text{atm}}(f,\theta) = S_{\text{out}}(f,\theta) + \frac{\rho_a}{\rho_w}\frac{\beta_{\max}}{\kappa^2}\exp(Z)Z^4\left(\frac{u'_*}{C}\right)^2 \times \max\{\cos(\theta-\theta_u),0\}^p \sigma F(f,\theta) \tag{8}$$

$\beta_{\max}$ is the non-dimensional wind-wave growth coefficient, $\rho_a$ and $\rho_w$ are the density of the air and water respectively, and $\kappa$ the von Karman constant. Then, $Z = log(\mu)$, where $\mu$ is the dimensionless critical height [40]. $C$ is the phase celerity and $u'_*$ is a frequency-dependent modified friction velocity used to reduce the wind input source term. $\theta$ and $\theta_u$ are the wave and wind directions respectively, and $\sigma$ the wave relative frequency observed from a reference frame moving with the mean current.

In Eq. (8) the second term on the right hand side is the wind input expression (adapted from [40]), and $S_{\text{out}}$ is the swell dissipation term representing the loss of energy to the atmosphere due to air-waves friction:

$$S_{\text{out}}(k,\theta) = r_{\text{vis}} S_{\text{out,vis}}(k,\theta) + r_{tur} S_{\text{out,tur}}(k,\theta) \tag{9}$$

In Eq. (9), $r_{\text{vis}}$ and $r_{\text{tur}}$ are 2 "weight" terms to give the relative importance of viscous and turbulent swell attenuation which effects are controlled by the ratio of the significant Reynolds Number Re and its critical value $\text{Re}_c$:

$$r_{\text{vis}} = \quad 0.5\left[1-\tanh\left((\text{Re}-\text{Re}_c)/s_7\right)\right] \tag{10}$$

$$r_{\text{tur}} = \quad 0.5\left[1+\tanh\left((\text{Re}-\text{Re}_c)/s_7\right)\right]. \tag{11}$$

with $\text{Re} = 2u_{\text{orb,s}}H_s/v_a$ (where $u_{\text{orb,s}}$ is the significant orbital velocity). Thus, the $S_{\text{out}}$ term includes the effects of the transitions from (linear) viscous to (nonlinear) turbulent boundary layer on the surface of waves, to account for the wave heights' Raleigh distribution. Particular adjustments are made to enhance the turbulent dissipation term ($S_{\text{out,tur}}$) in Eq. (9), which has the following form:

$$S_{\text{out,tur}} = \frac{\rho_a}{\rho_w}\left(16 f_e \sigma^2 u_{\text{orb}}/g\right) F(k,\theta) \tag{12}$$

with

$$f_e = s_1\left(f_{e,\text{GM}} + [|s3| + s2\cos(\theta-\theta_u)]u_*/u_{\text{orb}}\right) \tag{13}$$

In Eq. (11) and (10), $s_7$ is a "tunable" parameter used to increase or reduce the range of wave heights with turbulent boundary layers over groups of larger waves and viscous boundary layer over the groups of lowest waves [60].

The term $f_e$ included in Eq. (12), accounts for the adjustable effects of wind speed on the surface roughness. $f_{e,\text{GM}}$ is the friction factor from [61] for rough oscillatory boundary layer without a mean flow. Particularly in Eq. (13), $s_1$ is an adjustable parameter of O(1) that can be used to enhance the effect of turbulent swell dissipation.

### 3.4. Forcing fields and bathymetry

Waves are generated by winds, hence, wind fields are the main forcing input in the model. For the generation of this hindcast, the ECMWF ERA5 wind fields defined at 10 m above sea level are employed [13]. The ERA5 reanalysis was generated using 4D-Var data assimilation from the Integrated Forecast System (IFS) model cycle 41r2. This product presents 1-hourly $u$ and $v$ intensities components with a spatial resolution of 0.25°. ERA5 winds are used to force all grids in the proposed model setup (N_ATL-15M, N_ATL-8M and EU_ATL-2M).

At high latitudes, the ice coverage plays an important role in wave dumping and scattering. Particularly in the northern Arctic circle, seasonal changes in the ice coverage affect also the fetch extension for wave generation. To account for this effects, ice concentration data is taken from the Ifremer SSMI-derived daily product [62]. In the absence of a detailed database to define the ice thickness at the ice edge, a constant 1 m is considered.

Global currents can modify the wave fields due to changes in the relative wind, wave advection, and refraction effects specially in regions with strong current gradients [63]. As shown in [11,64], including global currents can help to improve the accuracy of the simulated sea states in those regions where the Total Surface Current Velocity (TSCV) is well represented. Additionally, Marechal and Ardhuin [65] showed the importance of utilizing spatial resolution ≤ 30 km in spectral models to properly account for refraction effects at global scales. This is aligned with the resolution used in the N_ATL-15M grid. Here, the CMEMS Globcurrent product is used (product MULTIOBS_GLO_PHY_REP_015_004). It includes the effects of geostrophic and Ekman components based on the method of Rio et al. [66]. Particularly, for the reconstruction of the geostrophic currents component, the CNES-CLS mean dynamic topography [67] is used. This product presents current fields each 3 h and has a spatial resolution of 0.25°. Global currents are only used as forcing in N_ATL-15M.

Within the European coastal shelf, tidal currents become dominant. Their intensities can be much larger that those of geostrophic nature, specially in areas like the English Channel, Northern Scotland and the Irish sea. Locally, tidal currents have similar effects over wave fields as those described for global scales (wave advection, current induced refraction). Additionally, at smaller scales, wave focusing and blocking, and induced breaking can occur when waves propagate against strong current jets with increasing velocities [63]. On the other hand, tidal levels are very important in shallow water regions or in those areas with large tidal amplitude regimes which effectively changes the waves' propagation conditions. In grids N_ATL-8M and EU_ATL-2M tidal currents and levels are included using the Atlantic European North West Shelf Ocean Physics Reanalysis product provided by Copernicus (NWSHELF_MULTIYEAR_PHY_004_009). This dataset covers the North-West European coastal shelf (longitudes −19.89° to 12.99°, and latitudes 40.07° to 65.00°), has 1-hourly data, and spatial resolution of ∼ 7 km (1/16°). Wave breaking induced by wave–current effects is also considered in the saturation-based dissipation term from [39] included in the ST4 parameterizations package.

It should be noted that full understanding of wave breaking is not yet accomplished. Although it was shown in [63] that the dissipation term from [39] gives the most reliable effects for wave–current induced breaking, there are other approaches that may be considered [68].

The bathymetry used in all grids from the model setup, is taken from the GEBCO 2021 global gridded bathymetric data [69]. This dataset has a 15 arc-second spatial resolution (400 m approx.).

## 4. Results

### 4.1. Parameterizations adjustment for the North-East Atlantic

The adjustment process follows the method proposed in [11] for global applications, in this case, utilized in a smaller region defined

**Table 2**
Parameters adjusted per test. $\beta_{\max}$, $s_7$ , $\mathrm{Re}_c$, $s_1$, $U_c$ and $x_c$ correspond to input parameters BETAMAX, SWELLF7, SWELLF4, SWELLF1, WCOR1 and WCOR2 in WW3. $U_c$ in m/s, is the wind speed threshold from which the wind intensity correction starts acting and $x_c$ is the correction factor (see eq. 6 in [11]).

| Test name | $\beta_{\max}$ | $s_7$ | $\mathrm{Re}_c$ | $s_1$ | $U_c$ | $x_c$ |
|---|---|---|---|---|---|---|
| T475 | 1.75 | $4.32 \times 10^5$ | $1.15 \times 10^5$ | 0.66 | 21 | 1.05 |
| Bm1.65-WC | 1.65 | $4.32 \times 10^5$ | $1.15 \times 10^5$ | 0.66 | 20.5 | 1.04 |
| Bm1.65-WC-s7-s4 | 1.65 | $3.60 \times 10^5$ | $0.90 \times 10^5$ | 0.66 | 20.5 | 1.04 |
| **TUD – 165** | 1.65 | $3.60 \times 10^5$ | $0.90 \times 10^5$ | 0.68 | 20.5 | 1.04 |

here as the North-East Atlantic. This sub-region covers longitudes −40° to 37.5° and latitudes 15° to 80° (North). To make sure that the changes introduced are aimed to improve the sea states' simulations in the area of interest only, the Mediterranean, Baltic and Black Sea are not taken into account in this analysis. For the tuning process, all model-altimeter comparisons are done with 1 year simulations, using model output from N_ATL-15M and Jason-2 (from CCI V3), and excluding altimeter data closer than 40 km from the coast. The latter restriction is included to avoid comparing with less well resolved wave heights (in coastal areas) due to the coarser resolution of N_ATL-15M. The Jason-2 altimeter is selected since it was used to inter calibrate the altimeter missions from the CCI dataset [70]. We take as a starting point the T475 parameterization values proposed in [11]. This includes the wind correction used to reduce the otherwise strong negative $H_s$ bias found for wave heights larger than 7 m when ERA5 winds are used. It should be noted that the set of parameters from T475 were defined mainly by minimizing the model-altimeter $H_s$ differences globally, using the Jason-2 altimeter data from the Sea State CCI V1 database [70].

The same year used to define T475 was selected to start the parameters' adjustments, 2011, which presents the highest wave heights recorded during February of that year [71]. This makes it suitable to perform model calibration including a wide range of sea states and to directly see differences with respect to the calibration done with Jason-2 from CCI V1. All parameter values used in the tests presented in this section are detailed in Table 2. All values not specified in this table are equal to those defined in T475.

We observe that, within the analyzed area, the use of T475 gives a positive $H_s$ bias of ∼5.5% within the range of the most frequent waves (2 m). This positive bias increases towards smaller wave heights (∼12% at 1.25 m) and it is of about 2% for $H_s$ from 3 to 5 m (Fig. 2.a). This general overestimation is first reduced by decreasing the $\beta_{\max}$ value to 1.65 and slightly adjusting the wind correction (Bm1.65-WC in Fig. 2.a). The reduction of $\beta_{\max}$ helps to correct the bias for $H_s$ in the range of 2.5 to 6 m to almost 0% in average, but there is still a clear positive bias for $H_s$ of 2 m and smaller. On the other hand, the change of the wind correction starting at 20.5 m/s helps to avoid the increase of the negative bias for $H_s > 7$ m.

To mitigate the positive bias still present for $H_s \leq 2$ m in Bm1.65-WC, the $s_7$ parameter was reduced to $3.6{\times}10^5$ as proposed originally for the T471 parameterization in [16]. Additionally, to enhance turbulent swell dissipation effects, the critical Reynolds $\mathrm{Re}_c$ was also reduced (Bm1.65-WC-s7-s4 in Fig. 2.a). Finally, it is noticed that a slight augment of the $S_{\mathrm{out,tur}}$ effect from Eq. (9), increasing $s_1$ to 0.68, helped to further reduce an extra ∼ 1.2% the bias for $Hs \leq 1.5$ m. This set of proposed values is called here parameterization TUD-165 ( Table 2).

Note that compared to T475, a bias reduction of about 5% is obtained for $H_s < 2$ m when TUD-165 is employed for the North-East Pacific. Obtaining also an almost constant −1.2% bias (approx.) for wave heights in the 2.5 to 6 m. Although this represents a significant improvement, a ∼ 2.5% increase in the negative NMB is observed in the 7.5 to 9.5 m range. It is also noticed that for $H_s$ <2 m there is a clear HH reduction of 2 to 2.5% with TUD-165 (Fig. 2.c). On the other hand, no significant changes of SI are observed for the full range of analyzed $H_s$ (Fig. 2.b). In [11] it was shown that adjustments in the swell dissipation parameterization through $s_7$ and $\mathrm{Re}_c$ have an effect in the shape of the $H_s$ distribution. This is due to the modifications introduced in the transition from a laminar to turbulent boundary layers above the waves, which is key to account for the Raleigh distribution. The changes applied, leading to TUD-165, are mainly aimed to reduce the $H_s$ bias for an extended range of wave heights and thus reduce uncertainties in the context of wave energy applications. Nevertheless, it is also necessary to verify their effects in the wave heights distribution. In Fig. 3.a is possible to see that, in general, all tests closely follow the distribution obtained with Jason-2. In fact, most interesting changes observed with TUD-165, are introduced only for $H_s$ between 1 to 1.5 m with a small reduction of the occurrences underestimation e.g. ∼ 1% at 1.25 m, and a slight increase of the over estimation of occurrences at 1.75 m compared to T475 (∼ 0.75%; Fig. 3.b).

The overall positive bias of $H_s$ observed with T475 (Fig. 2.a) is attributed to the overestimation of wave heights from the CCI V1 Jason-2 data compared to offshore buoy measurements [70]. The correction of this bias in the CCI V3 dataset, is one of the main reasons for the $\beta_{\max}$ reduction applied in TUD-165 to decrease the $H_s$ NMB in the bulk of the simulated data. Another important aspect to take into account, is that the wave retracking algorithms to estimate SWH used in CCI V1 and CCI V3 are different. While retracking algorithms like ALES [72] or Brown-Peaky (BP; [73]) are used in CCI V1, WHALES is employed in V3 [29,30]. The differences observed in the Jason-2 SWH distributions between CCI V1 and CCI V3 are thought to be mainly related to these algorithms (Fig. 4.a). It is then expected that, depending on the dataset employed as reference, different swell dissipation adjustments will be required to better represent the observed $H_s$ distributions, as it happens with T475 compared to CCI V1 and TUD-165 compared to CCI V3 (Fig. 4.b).

### 4.2. *TUD-165 verification with merged altimeter tracks and buoy data*

So far, the effect of adjustments leading to TUD-165 have only been assessed in terms of wave height comparisons between WW3 and Jason-2 at "basin scale". While satellite altimetry allows to estimate the model performance with a wide spatial coverage, buoy data typically provides other wave parameters (besides $H_s$) with higher density of measurements at specific locations.

To evaluate the performance of TUD-165 spatially, the $H_s$ NMB and SI are computed with the higher resolution output from N_ATL-8M and the integrated tracks from Jason-1, Jason-2 and Envisat. Using a higher resolution grid helps to better capture the wave field's changes within the coastal shelf. This is specially important in areas where depth-induced refraction and wave–tidal current interactions become dominant [26]. Incorporating different altimeter missions helps to increase the measurements density within the analyzed area. It also increases the number of repetitions in those places crossed by multiple altimeter tracks.

In Fig. 5.a, it is possible to observed that outside the coastal shelf, at depths > 500 m, the $H_s$ NMB is typically ≤ 5 %, with the exception of the southern Bay of Biscay where NMB can reach 10 %. Within the European coastal shelf we found areas with higher NMB values. Again, the southern end of the Bay of Biscay presents a bias that can reach ∼ 10%. Similar results are observed in some parts of the Irish Sea. The North Sea stands out as a zone with low NMB, typically below 5%. The highest bias values are found between The Hebrides and Scotland, the south-western end of the English Channel and the Danish straits. Note that these areas also present larger SI (≥ 16 %; Fig. 5.b). For these particular cases, it is thought that the larger NMB and SI are related to the high noise to signal ratio in the altimeters' measurements close to land. The detection of (non Gaussian) land surface might interfere with the retrieval of the geophysical signal of waves in the radar footprint, which in the end leads to errors in the estimation of the SWH.

In terms of the SI, outside the mentioned areas with high values, it is observed that, in general, this parameter ranges from 10% to 12%

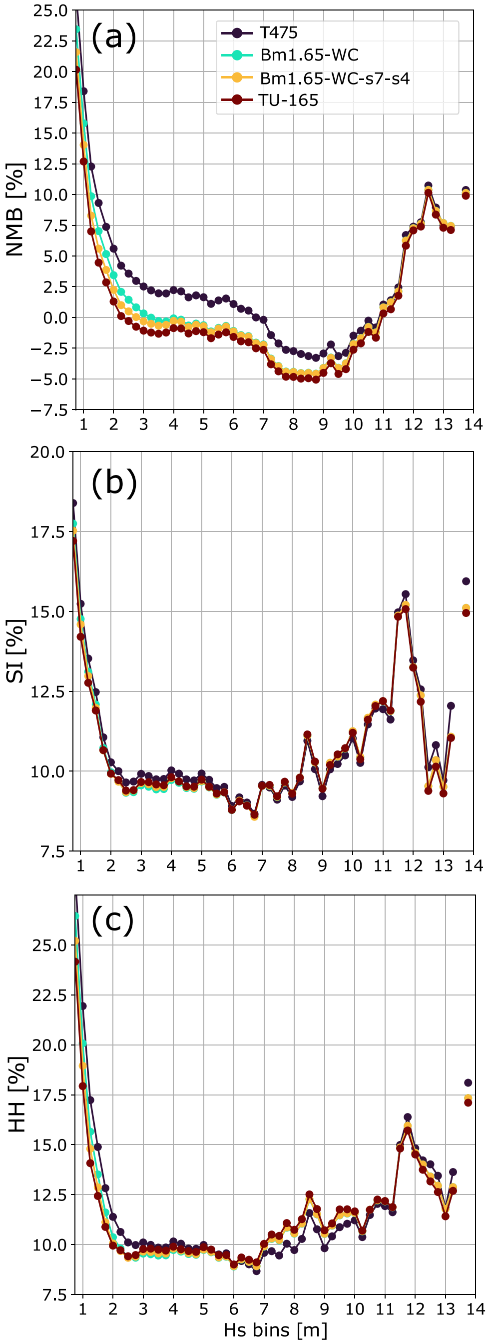

**Fig. 2.** Performance parameters for model adjustment tests (WW3 - Jason-2). Analyzed year: 2011. (a) $H_s$ normalized mean bias (NMB), (b) scatter index (SI), and (c) Hanna and Heinold index (HH). $H_s$ bins width is 0.25 m.

within the analyzed region (Fig. 5.b). These results are aligned with the findings from [26] on the performance of unstructured grids.

Although the results from Fig. 5 give a good overview of the model performance using TUD-165 (for the complete domain), it is still of interest to verify the model accuracy with in situ measurements. Buoys provide records of a wider range of sea states at specific locations, offer more wave variables than satellites, and are normally more accurate for measuring wave heights < 1 m. Here, a set of 34 buoys from Table 1 are used as reference to compare $H_s$, $T_p$ and the mean wave period $T_{02}$ from the 2011 1-year simulation. Results for the NMB, BIAS, SI and CORR (Pearson correlation coefficient) related to these wave parameters are presented in Fig. 6.

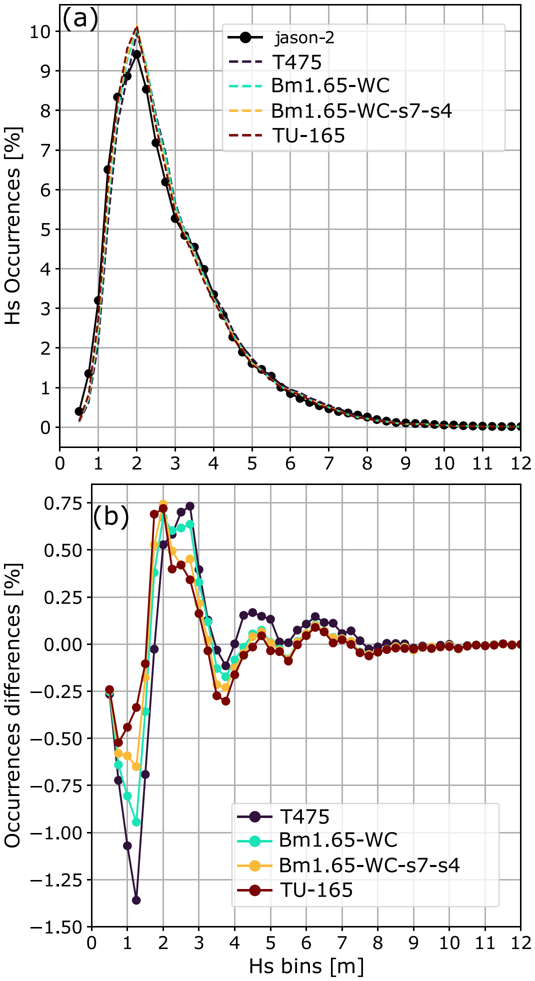

**Fig. 3.** $H_s$ normalized distributions for parameters adjustment tests. Analyzed year: 2011. (a) $H_s$ occurrences normalized by total amount of data (1,113,727). (b) Normalized occurrences differences with respect to Jason-2 CCI V3 (WW3 - Jason-2).

The first interesting feature noticed, is that the wave heights' NMB in the southern side of the Bay of Biscay, is smaller than previously estimated with altimeter data (Fig. 5.a). Results in Fig. 6.a show that the $H_s$ NMB ranges between −4.2 and 6.5%. In general, for most locations, the NMB is well constrained between −5 to 5% (equivalent to a bias range of −0.2 to 0.2 m). There are 2 locations, in the English Channel, with the highest NMB for $H_s$, 35% at buoy 6200103 and 19.5% at 6200027, which corresponds to 0.46 and 0.26 m respectively. The highest wave heights' SI are also observed at these locations (19.3% at 6200103 and 16.6% at 6200027). It is thought that main source of these over estimations and errors are related to the combined effects of inadequate spacial resolution of the tidal and wind forcing. The combined effect might lead to an overestimation of the effective wind. It is also possible that there is induced wind variability due to inaccuracies of the modeled atmospheric boundary layer development as it transitions from water to land (or land to water).

In general, the $H_s$ SI obtained with buoy data follows the spatial distribution obtained with the altimeters (Fig. 5.b). Nevertheless, results at buoy L91, close to the Dutch coast, show a lower SI (12.8%) than the estimations with altimeters' data (∼ 18%). In terms of $H_s$ correlations (CORR), values > 0.95 were obtained for most locations, with exception of Donostia-buoy (off the coast of San Sebastian) where CORR = 0.92. These results point to an overall good simulation of the wave heights evolution, closely following the recorded $H_s$ time series.

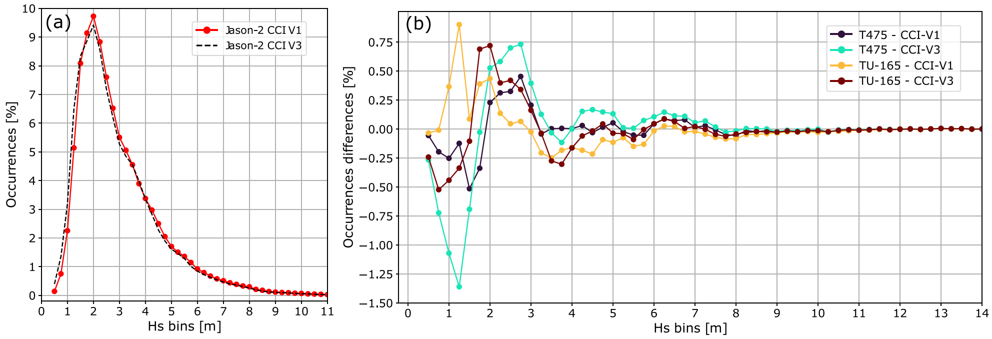

**Fig. 4.** (a) Jason-2 $H_s$ normalized distributions from CCI V1 and V3 datasets. (b) Normalized occurrences differences with respect to CCI V1 and V3 (WW3 - Jason-2). Analyzed year: 2011.

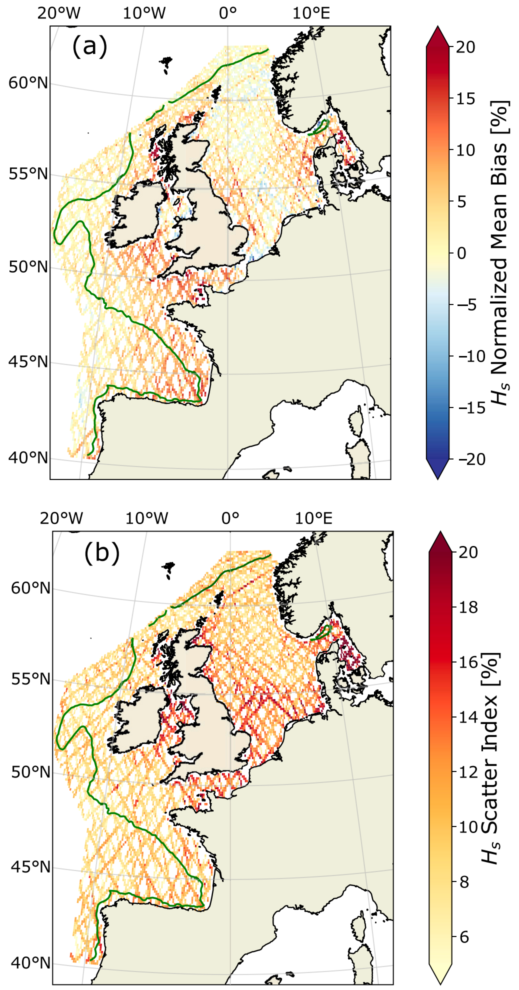

**Fig. 5.** (a) Normalized Mean Bias (NMB) and (b) Scatter Index (SI) estimated with Jason-1, Jason-2 and Envisat for TUD-165, year 2011. Altimeter measurements closer than 12 km from coastlines are not considered in the analysis. Green continuous lines indicate the 500 m depth contours.

In Fig. 6.b the model performance results for $T_p$ are shown. Peak period from buoy measurement typically present high temporal variability, related to its dependence on the local wind conditions. In addition, one must take into account the instruments' accuracy and sampling rate. This temporal variability is not properly captured in spectral models, which is mainly due to the wind forcing field characteristics (e.g.; spatial and time resolution) and the wave nonlinear interactions parameterization (e.g.; DIA or GQM method). Additionally the frequencies discretization of the spectrum play significant role on where the peak period is estimated. To reduce the high time variability from the buoy measurements, a moving average with 2-hour window was applied to the $T_p$ time series.

As can be observed in Fig. 6.b, only half of the analyzed buoys present $T_p$ information. With the exception of Donostia-buoy, the largest $T_p$ bias are obtained when comparing the model simulations with buoys from Puertos del Estado. At these sites (6200024, 6200025, 6200083, and 6200084), the $T_p$ NMB is in average 14% (approx. 1.2 s), while for all other locations the NMB ranges between −2.8 to 2%. For the peak periods SI, the highest values are found in the North Sea, with values of 20, 21.9 and 24.7% at the locations of buoys D151, J61 and NsbIII respectively. At these places some of the lowest correlations are also observed. It was found that these low SI and CORR values are mostly related to differences in the estimation of the peak period during low energetic sea states. Basically, during sea states with very low $H_s$. An example at the location of buoy J61 is presented in Fig. 7. Here it is possible to observe that, even though the simulated $H_s$ time series closely follows the buoy data, big "jumps" of the modeled $T_p$ are detected. These jumps occur when there is a reduction on the $H_s$ (from an already low energy sea state), related to a slight drop on the wind conditions (Fig. 7.a). It is possible that the model takes longer to put energy in the development of the wind sea under low wind intensities conditions. As a results, the peak of energy corresponds to a swell component with longer periods. This can be observed in Fig. 7.b, around 2011-05-31 between 03:00 and 11:00, or the first half of the day on 2011-06-01. It is also possible that the forcing wind is too mild and thus the local wind sea develops with less energy. In the absence of spectral data from the buoy, it is difficult to properly assess the sources of this effect.

Finally, the wave mean period $T_{02}$ is analyzed (Fig. 6.c). As for the peak period, it is observed that the largest NMB, is obtained at the location of buoys 6200024, 6200025, 6200083, and 6200084. For the $T_{02}$ the NMB ranges between 11 to 18%, equivalent to 0.7 to 1.2 s. The largest underestimation of $T_{02}$ is found in the English Channel when comparing with buoys 6200103 and 6200027, reaching −26 and -35% respectively. Particularly at these locations, the comparison of the model results was done with the mean zero crossing period ($T_z$) from the buoys. Its suitability can be argued since it is not obtained from the integration of the spectrum, but it was still considered as a reference. For the rest of the domain the NMB ranges between −3.5 to 5.5%.

The $T_{02}$ SI typically goes from 7 to 12% in most locations, with exception of the already mentioned sites 6200103 and 6200027, and at buoy 6300110. In fact, the highest SI is obtained when comparing with the latter one (19.7%), which might be misleading, since it was also obtained using $T_z$. Note how at 6300112, immediately to the North, the SI is only 8.2%. Correlations between the mean periods from simulations and measurements are, in general, significantly higher than those obtained for $T_p$. This is expected since the evolution of

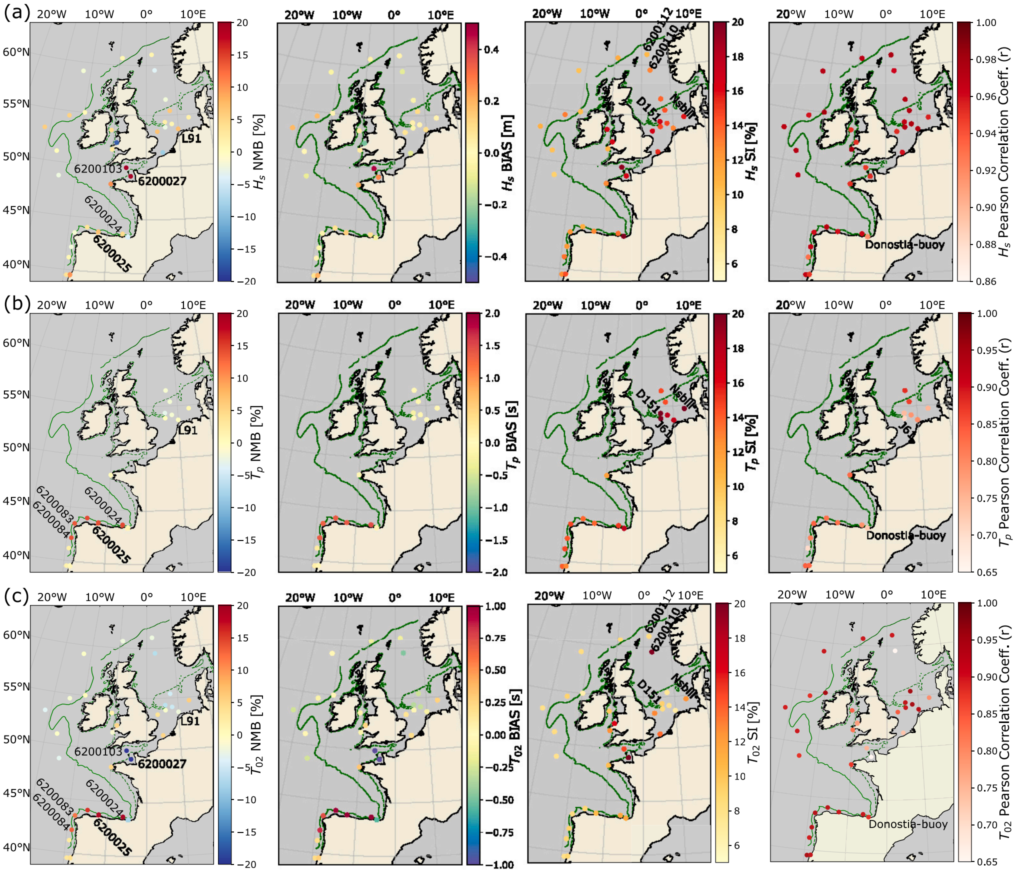

**Fig. 6.** Normalized Mean Bias (NMB) Bias, Scatter Index (SI) and Pearson correlation for (a) $H_s$, (b) $T_p$, and (c) $T_{02}$. Results for 2011 (1 year simulation) using TUD-165. All parameters computed between WW3 output files at the locations of the buoys listed in Table 1 (WW3-Buoy). Green lines indicate the 500 m depth contours and dashed green lines the 50 m depth contours obtained from the N_ATL-8M grid. Buoys' names at each location in Fig. B.14.

parameters obtained from integration of the spectrum (like $H_s$), are better represented in the model. Again with the exception of buoys 6200103, 6200027 and 6300110, CORR values range from 0.75 to 0.94. Particularly high correlation values are observed off the coast of Portugal and Spain, with values $> 0.90$.

### 4.3. Hindcast validation

#### 4.3.1. Validation with altimeter data

So far, the performance of the results obtained using TUD-165 have been assessed for the "tuning" year (2011) only. The along-track type analysis, to verify accuracy of the modeled $H_s$ fields, was done using Jason-2 only for the parameters adjustment phase (Section 4.1).

To provide a better idea of the range of NMB, SI, and HH index values for different wave heights, model validation is done using all available years from 5 different altimeter missions (2008–2019): Envisat (2002 to 2012), Jason-1 (2002 to 2012), Jason-2 (2008 to 2019), Jason-3 (2016 to 2020) and Saral (2013 to 2018). With this, the full time window of altimeter data provided by the CCI V3 dataset is covered. $H_s$ fields from the N_ATL-8M are used to compare with altimeters data. Additionally, altimeter data closer than 12 km from the coast are not considered in the analysis.

First, to provide an example of the inter annual variability of the model accuracy levels, the NMB and SI obtained for each year from 2008 to 2019 using Jason-2, is shown in Fig. 8. This yearly analysis gives a good idea of the range of changes in the model accuracy, that can be expected for different wave height values. In the neighborhood of the most frequent wave heights (1.5 to 2.5 m), variation in the NMB is $\leq 2\%$. This range increases towards larger $H_s$, reaching a variability $\leq 4.0\%$ between wave heights of 2.75 to 6.5 m, and can be of about 9% in some cases for wave heights $> 7$ m (Fig. 8.a). This overall behavior is also observed for the SI, although changes are more constrained (Fig. 8.b). The variability range of the SI for the most frequent wave heights is $\leq 1.2\%$, increases up to 2.5% for wave heights of 2.75 to 6.5 m, and can be of about 8% for $H_s = 9.75$ m.

Comparing only the NMB of year 2011 obtained in Figs. 2.a and 8.a, some differences can be found. In the latter one, there is a slight shift of NMB to positive values ($\sim 1.5\%$) for $H_s \leq 3$ m and also a reduction of the under estimation of wave height $> 7$ m. It is possible that the main source of this differences is the use of altimeter data closer to the coast down to 12 km offshore. Also, the higher resolution of the N_ATL-8M grid used for the analysis in Fig. 8, which helps to better represent the wave field evolution within the European coastal shelf.

Finally, it is of interest to also verify how the estimation of the performance parameters might change when the modeled $H_s$ fields are compared with different altimeters. Different instruments, with their own measuring characteristics, might have specific accuracy levels. Thus, validation with a set of altimeters provide further information on the accuracy ranges of the generated hindcast. In Fig. 9 the $H_s$ NMB, SI and HH index are computed using all available years from each selected altimeter mission, with exception of Saral. Although the CCI V3 dataset provides Saral data until 2021, we have used data only until year 2018, 2 years into its drifting phase [74]. This rather conservative approach is used to ensure the quality of the data from this particular altimeter [75].

In Fig. 9.a, it is possible to observe that the NMB for $H_s$ between 1.25 to 6 m, obtained with all selected altimeters is very similar, with a differences range $\leq 2\%$. This range is kept for larger wave heights up to 9.5 m, with the exception of Jason-3 which in general gives a slight

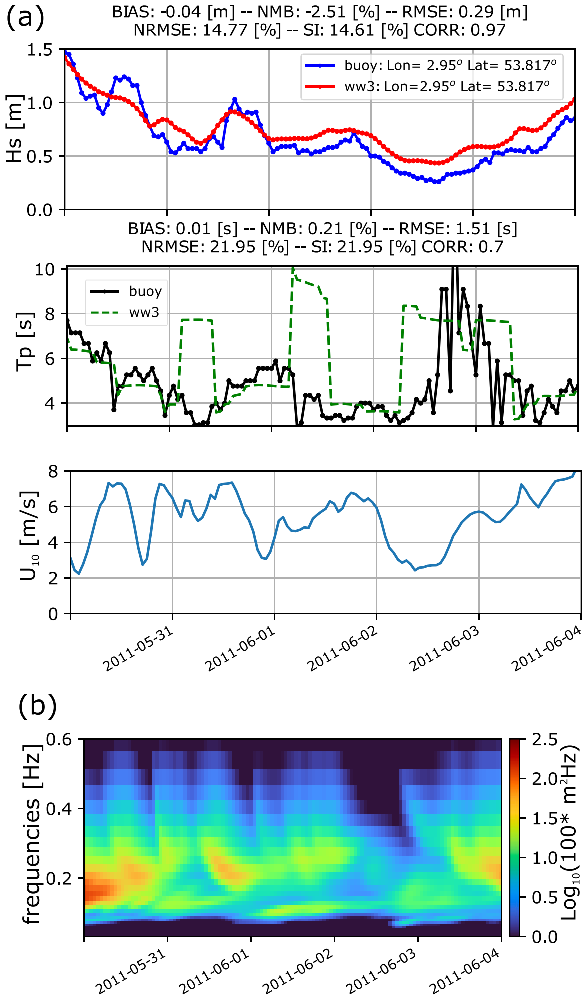

**Fig. 7.** (a) Time series detail of recorded and modeled $H_s$ and $T_p$ on top and middle panel, and wind intensity as read in the model on bottom panel. (b) Time series of the modeled wave spectra. The buoy $T_p$ time series does not include the 2-hours time window moving average.

wave heights over estimation of 1.5 to 3%. Different behaviors are observed for the largest wave heights ($> 10$ m), specially when looking at the results obtained with Jason-1. When model results are compared with the latter one, it gives the largest overestimation (NMB = 14%) at $H_s = 11.25$ m. Jason-2 and Envisat show a more similar behavior, with estimated NMB levels that are comparable with differences range $< 3.5\%$.

The wave heights' SI and HH index present similar values (Fig. 9.b, c). In this case, there is a clear difference between the curve obtained with Jason-1, for wave heights $> 10$ m, compared to the other 4 altimeters (Envisat, Jason-2, Jason-3 and Saral).

### 4.3.2. Validation with buoy data

All the adjustments and part of the hindcast's validation have been done only in terms of wave parameters like $H_s$ and $T_{02}$. Here, a brief analysis of the spectral energy distribution is included to provide further details on the model performance using TUD-165. Four buoys with spectral data, within the Bay of Biscay are selected to compare with output from the model requested at those locations: 6200001, 6200069, 6200080 and 6200066 (see Table 1). The year 2020 was selected since the 4 buoys presented simultaneous measurements throughout the year. First, all buoy data was interpolated into the discrete frequencies used in the WW3 implementation, and time-matched with the output files requested at those locations. Then, the mean spectral energy values at each frequency are computed for 1 year, and the model-buoy mean difference is computed. This provides information on where the simulated spectra under or overestimates the energy levels (Fig. 10.a). To give an idea on changes of the model accuracy related to seasonality, the same analysis is computed over 2 different time windows: January–February and July–August. These periods were selected to visualize changes in the simulated energy distribution under the effect of strong and mild wind conditions during winter and summer respectively (Fig. 10.b).

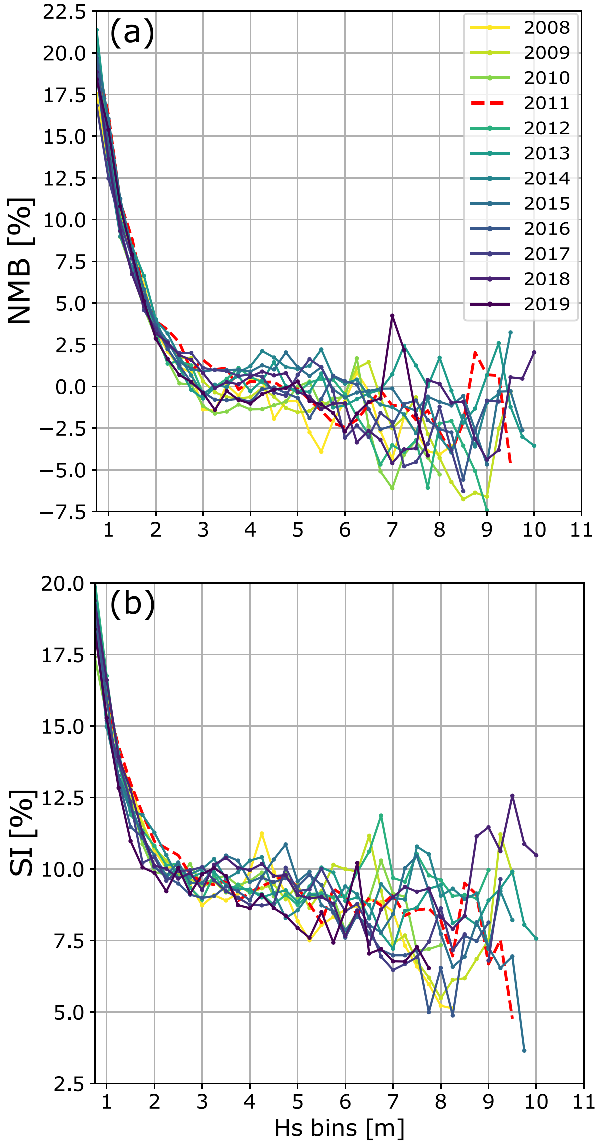

**Fig. 8.** Inter-annual variability of model performance using Jason-2. (a) $H_s$ normalized mean bias (NMB) and (b) Scatter Index (SI). Year used for model calibration (2011) in dashed red line. $H_s$ bin size is 0.25 m.

The smallest differences of the annual spectral energy mean are found at buoys 6200001 and 6200080, located at deep and intermediate waters respectively. The largest differences, due to an overestimation of the mean spectral energy are found at buoy 6200066, reaching 3 m$^{2\ \text{Hz}}$. At 6200069, there is a clear "shift" to lower frequencies of the mean energy curve compared to the in situ data. This behavior was also observed for year 2021 (not shown), but with smaller deviations. In general, at all locations, most noticeable differences are found at frequencies $< 0.1$ Hz (Fig. 10.a).

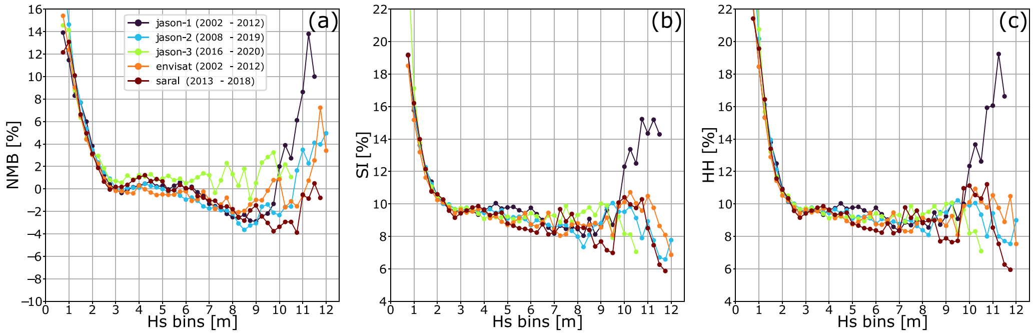

**Fig. 9.** Validation parameters obtained for different altimeter missions. (a) $H_s$ normalized mean bias (NMB) and (b) Scatter Index (SI) and (c) Hanna and Heinold index (HH). $H_s$ bin size is 0.25 m. Altimeter measurements closer than 12 km to the coast are not considered. Statistical parameters are computed with at least 50 occurrences per wave height bin.

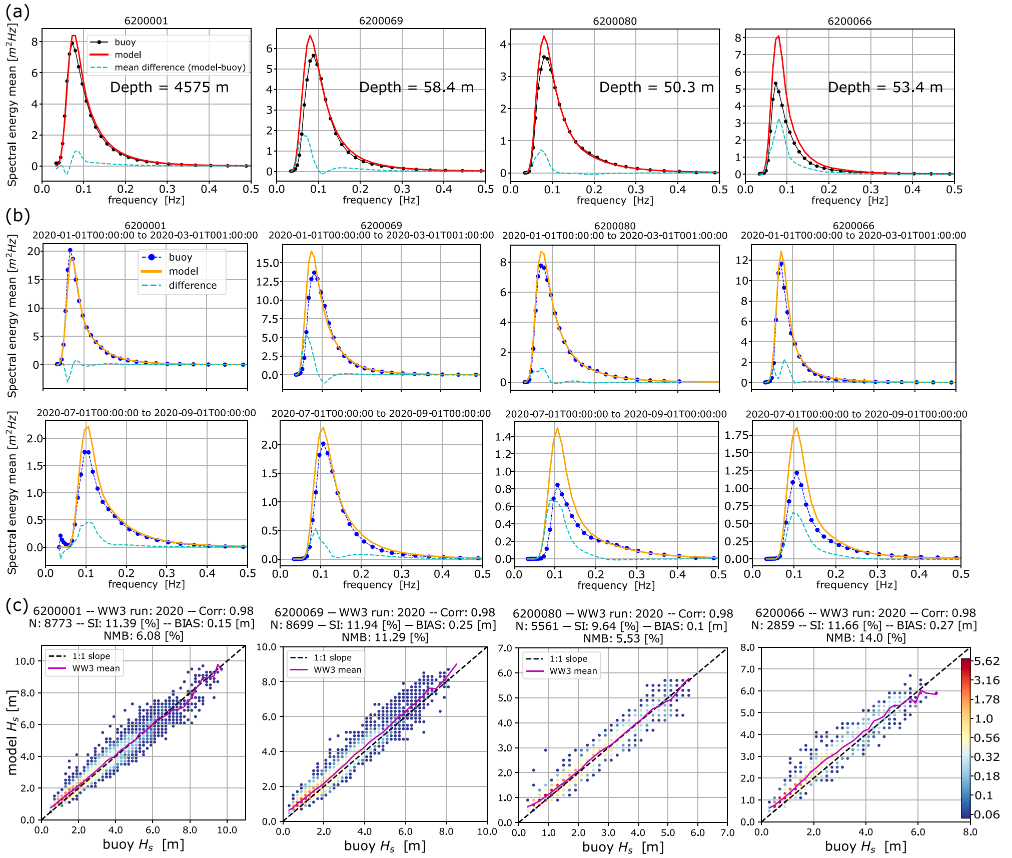

**Fig. 10.** (a) Spectral energy mean comparison for 2020 at buoys 6200001, 6200069, 6200080 and 6200066. (b) Same as (a) but for January–February (top panel) and July–August (bottom panel). (c) Scatter plot and performance parameters of $H_s$. Colorbar in (c) indicates normalized occurrences in % (N is the total amount of model-buoy time-matched data).

With the exception of 6200069, simulations present mean spectral energy distributions that closely follow the measurements during winter months, where stronger wind conditions are found (Fig. 10.b, top panel). In contrast, larger differences, related to overestimation of the mean spectral energy, appear during summer months with softer winds (Fig. 10.b, bottom panel). Results at 6200001, in deep waters, suggest that these could be related to a "high" $\beta_{\max}$ well balanced with the overall dissipation across the spectrum. This might favor the simulation of more energetic sea states and the development of longer waves (as in winter time), but leads to a non-negligible overestimation of the spectral energy for milder sea states. Particularly at 6200001, it is thought that this could explain the slightly high mean modeled wave heights for $H_s < 2$ m (Fig. 10.c).

At the location of buoys 6200080 and 6200066, where the largest energy overestimation is found for summer months, other processes are expected to play a more dominant role. Mainly refraction and dissipation induced by bottom friction. The excess of spectral energy in the neighborhood of 0.1 Hz can be partially reduced with a higher bottom friction. Bottom friction dissipation might be particularly important at 6200080, located about 130 km away from the edge of the coastal shelf (towards the coast).

Directionality of the incoming waves might also play an important role. Some (longer) wave components arriving from the NW to the Bay of Biscay (to 6200080), travel longer distances over the continental shelf. Thus, the cumulative effect of dissipation due to bottom friction becomes more important (e.g; [76]). Nevertheless, when analyzing $H_s$, comparisons between the model with the buoy 6200080 still show

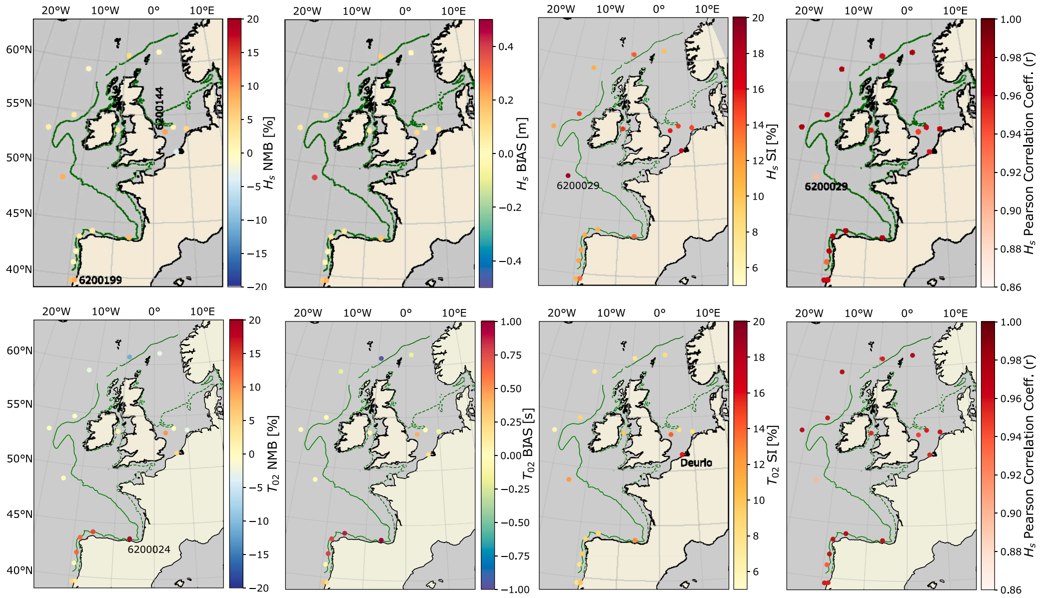

**Fig. 11.** (a) Normalized Mean Bias (NMB), Bias, Scatter Index (SI) and Pearson correlation for (a) $H_s$ and (b) $T_{02}$. Results for 2020 (1 year simulation) using TUD-165. All parameters computed between WW3 output files at the locations of the buoys listed in Table 1 (WW3-Buoy). Green lines indicate the 500 m depth contours and dashed green lines the 50 m depth contours obtained from the N_ATL-8M grid.

a high correlation (0.98) and low bias (NMB = 5.5%) for the bulk of the data (Fig. 10.c). Similar results were observed for the mean period $T_{02}$ (not shown). This is not the case at 6200066, where the highest $H_s$ NMB is found for the bulk of the data (NMB = 14%, and similar for 2021). Although at this location the mean spectral energy from winter months is closer to the buoy mean, there is still a larger overestimation close to 0.07 Hz ($\sim$ 2 $\mathrm{m}^{2\ \mathrm{Hz}}$). That larger amount of energy at longer wave components is not observed at 6200080. It is thought that this is one of the main reasons for the higher mean $H_s$ values across the analyzed wave height range at 6200066 (Fig. 10.c, magenta line). Further analysis should be carried out in this area for both, the buoy data quality, and the effects of offshore wave incidence to verify potential influence on the refraction representation.

TUD-165 is slightly different to parameterization T475 [11], and most changes have been introduced to swell dissipation and wind input terms. It is thus expected that directional characteristics of the spectrum (e.g.; directional spreading), perform similar to those of T475.

To compare with previous results obtained for 2011 (Fig. 6), a similar performance analysis was performed, for $H_s$ and $T_{02}$, with the available in situ data for 2020 (Fig. 11). Overall the bias, SI and high CORR levels are maintained. For example at buoys 6200199 an 6200144, the $H_s$ NMB is $\tilde{8}.5$%. The $H_s$ SI for 6200029 is particularly high for 2020 (18.9%), which is suspected to be an artifact of the instrument. Still, a high correlation level of 0.9 is obtained. The highest $T_{02}$ is found at 6200024 (19%), as observed in 2011. This over estimation could be related to an excess of spectral energy obtained for frequencies $< 0.1$ Hz in that particular area, as observed at 6200066 (Fig. 10).

The overall range of values obtained for the performance parameters used for 2020 and previous years (not shown), suggest that the model results are consistent in time. It also shows that the results previously presented in Section 4.2 for the "tuning" year, are representative of the expected accuracy levels from the generated dataset.

### *4.4. Comparing ECHOWAVE with ERA5 and WAVERYS*

To further analyze the performance of the ECHOWAVE hindcast, it is of interest to compare with current available wave datasets. The WAVERYS and ERA5 wave products are selected for this purpose. All performance parameters are computed using the Jason-3 altimeter data from 2016 to 2020 (within the North-East Atlantic, as defined in Section 4.1). Since WAVERYS and ERA5 are global wave datasets, with spatial resolutions of 0.2° and 0.5° respectively, it is adequate to perform the datasets comparison using the N_ATL-15 grid from ECHOWAVE (spatial resolution of 0.25°). Given the coarser resolution from the ERA5 wave product, only wave data further than 50 km from the coast line was considered for this analysis.

The 3 datasets present similar $H_s$ bias levels in the neighborhood of 2 m wave heights, close to 0%. While this level of NMB is fairly consistent up to $H_s$ of 5.5 m for ECHOWAVE, ERA5 shows a progressive increase of the underestimation of wave heights reaching −2.5% at 5.5 m. On the other hand, WAVERYS presents a slight overestimation in this wave heights' range (in average NMB  1.5%). It is also observed that for $H_s > 9$ m the ECHOWAVE hindcast performs better than WAVERYS and ERA5 that tend to underestimate larger wave heights, with NMB values of −5% at $H_s$ of 12 m (Fig. 12.a).

The $H_s$ scatter index from ECHOWAVE is higher than the other 2 datasets, for the complete range of analyzed wave heights. This is expected since WAVERYS and ERA5 are reanalyses that incorporate data assimilation from altimeters. Particularly, WAVERYS included Jason-3 in the assimilation process. Nevertheless, the $H_s$ SI from ECHOWAVE is, in average, just $\sim$ 4% higher than WAVERYS and about 2.5% higher than the ERA5 wave product (Fig. 12.b).

The significant wave heights' distributions of WAVERYS and ECHOWAVE are practically the same, and both closely follow the distribution obtained with Jason-3 for deep waters (or > 50 km away from the coast). In contrast, the ERA5 dataset presents a clear over estimation of occurrences of the most frequent wave heights (Fig. 12.c).

Global models with the accuracy levels of WAVERYS or ECHOWAVE's N_ATL-15M grid can provide a good overview of the wave field characteristics in deep waters. However, due to the coarse resolution, most of the wave field changes in shallower areas are not well represented. Alday et al. [26] showed the importance of higher resolution to better simulate the wave field propagation within the European coastal shelf. With this in mind, the performance results from the N_ATL-8M grid have been included in Fig. 12 to show the differences between accuracy levels at "global" scales, and within the coastal shelf. Particularly interesting are the lower SI values for $H_s > 6.5$ m, and the different $H_s$ occurrences distribution obtained

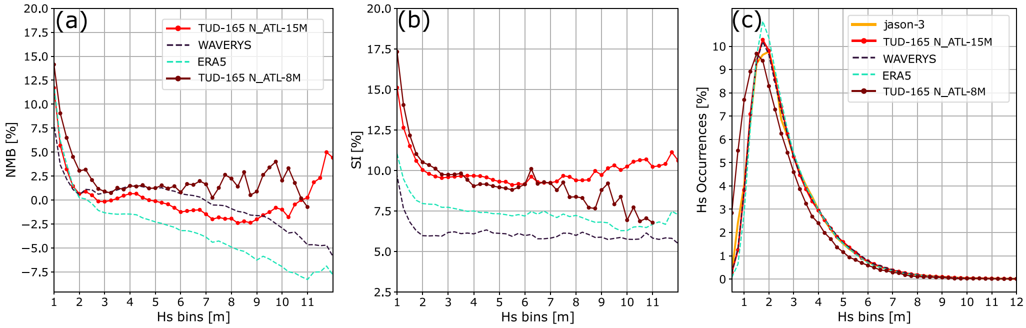

**Fig. 12.** Comparison between ECHOWAVE (TUD-165), WAVERYS and ERA wave product with Jason-3 from CCI V3. (a) $H_s$ Normalized Mean Bias (NMB), (b) Scatter Index (SI), and (c) $H_s$ occurrences distribution. Results computed using data from 2016 to 2020 (model - altimeter). $H_s$ bin size is 0.25 m.

with N_ATL-8M (Fig. 12.b and c). The PDF shape with the peak of occurrences shifted towards 1.5 m is only possible to capture thanks to the higher spatial resolution. This helps to improve the representation of the spatial changes of the $H_s$ fields, and allows the inclusion of data closer to the coast (12 km offshore) in the analysis.

### 4.5. Estimation of the wave energy flux

The main objective of the generated hindcast is to provide reliable high-resolution data for wave energy applications. It is thus necessary to evaluate the characteristics of the wave energy flux (pWave) within the European coastal shelf using ECHOWAVE. The 20-years (2001 to 2020) mean pWave is first computed using the EU_ATL-2M grid (Fig. 13.a). Then, the mean differences (Fig. 13.b) and normalized mean differences (NMD; Fig. 13.c) are estimated between WAVERYS and the EU_ATL-2M grid. This is done to quantify the effects of solving the wave field with higher resolution in shallower areas. To perform the comparison, the $H_s$ and $T_p$ fields from WAVERYS are interpolated into a finer grid matching the coordinated of the grid nodes from EU_ATL-2M. The wave energy flux (pWave) is then computed using the expressions detailed in Section 2.3.

It should be noticed that the area covered in the EU_ATL-2M high-resolution grid includes most of the locations of interest for deployments of WECs in Europe and the UK.

The 20 years mean pWave estimated with EU_ATL-2M provides a detailed characterization of the wave resource availability in coastal areas. Note that, when compared with WAVERYS, the largest differences (> 15 kW/m), are observed along the coasts of Portugal, Ireland, and the western coast of the UK. These differences show an underestimation of the wave energy flux that can be larger than −25% when global coarse models are employed for a resource assessment. It is also important to highlight that the largest differences are observed for depths ≤ 100 m. These are typical depths considered for offshore deployments of WECs (e.g.; [77]), particularly for point absorbers moored to the sea bottom .

Within the North Sea, the mean pWave is considerably lower than those areas directly exposed to swells and storms from the North Atlantic. The 20-years mean energy flux off the coast of The Netherlands an Germany is of about 9 to 10 kW/m (and smaller towards the English Channel). In this area the estimated pWave underestimation with WAVERYS can be ≥ −20%.

## 5. Discussion

Model validation with altimeter data shows that the largest interannual variability on the estimated accuracy, when comparing with altimeter data, is found for $H_s > 7$ m (Fig. 8). It is possible that this is due to the rather crude wind intensities correction applied to mitigate the underestimation of larger wave heights. Particularly, a slight increase of the SI was already observed in [11] (at global scale) for different wind intensities correction tests. This could also be attributed to the changing accuracy of the wind forcing field related to the amount of assimilated data (ranging between 0.75 million per day in 1979 to ∼ 24 million in 2018). Nevertheless, when analyzing longer periods of time, results suggest that in general the reduction of the underestimation of large wave heights is accomplished, with NMB levels ≤ −4%. Moreover, regardless of some high values observed in Fig. 8.a or Fig. 2.a for the largest wave heights, their overestimation is ≤ 6% when looking at longer time windows with different altimeters.

In particular, the clear different behavior of SI and HH obtained comparing with Jason-1, could be attributed to its inaccuracies for estimating larger wave heights [78]. Overall, considering Jason-2, Jason-3 and Saral, the SI and HH is well constrained to levels ≤ 10% for wave heights in the 2 to 12 m range when time windows > 4 years are considered (Fig. 9.b,c).

Interesting differences were found in the wave height distributions when comparing data from the CCI V1 and V3 datasets (Fig. 4). Depending on the dataset used, the selection of the swell (turbulent and laminar) dissipation terms to account for the Raleigh distribution of waves will change. In the absence of more reliable descriptions of the waves' boundary layers, we still rely on the mechanism included in the swell dissipation parameterization, and in the use of wave heights distributions for adjustments.

When analyzing spectral energy distributions, it was observed that TUD-165 performs better during winter months, were the majority of wave energy production potential is most interesting (Fig. 10.b, top panel). It is thought that this is related to a better balance between the wind input and wave breaking source terms. Particularly, non-negligible overestimation of wave energy was found during summer months in South of the Bay of Biscay. It is suspected that the effects of bottom friction are underestimated over the coastal shelf within the Bay of Biscay. It is also possible that inaccurate refraction effects (wave focusing) might lead to an excess of energy in the southern side of this area. This should be further investigated taking into account offshore wave incidence, directional discretization, refraction time step from the model, and the local energy levels (at buoy 6200066 for example).

Sometimes the impact of inaccuracies of the spectral energy are compensated when it comes to the estimation of wave parameters obtained from the integration of the spectrum. In extent, this might have only a mild effect in bulk estimations of the mean wave power density resource. When it comes to the simulation of WEC responses, and computations of the absorbed and produced power, accurate representation of the spectral energy levels is of great importance. It is thus necessary to further evaluate the accuracy of the presented hindcast in terms of spectral energy for different locations (outside the Bay of Biscay). Efforts to obtain spectral in situ data are considered for future related studies of this subject.

The low and constrained biases obtained, make this database one of the most suitable for wave energy applications. The effective ranges of wave energy production for most wave energy converters (WECs),

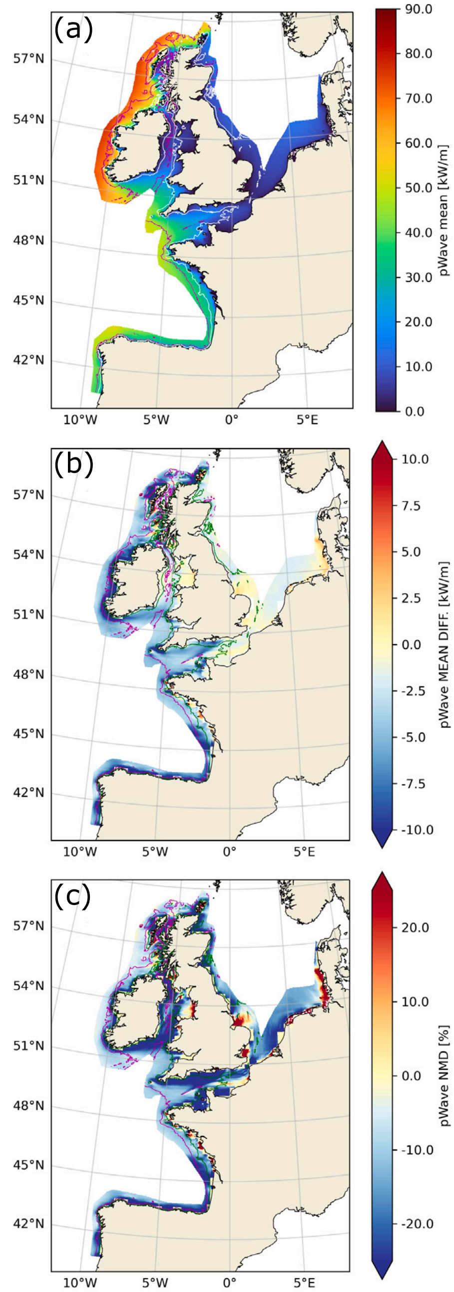

**Fig. 13.** 20 years mean wave energy flux comparison between WAVERYS and ECHOWAVE EU_ATL-2M grid. (a) Mean pWave from ECHOWAVE, (b) pWave mean difference, and (c) pWave normalized mean difference. Differences computed as WAVERYS-ECHOWAVE. Magenta lines show the 200 m depth contour, white and green lines the 50 m depth contour.

are within 2–6 m $H_s$. Whilst higher NMB is observed for $H_s \geq 9$ m, these are ranges where the majority of wave energy converters go into survival mode and produce no power. At the same time, the reduced bias obtained for the largest wave heights, when compared with measurements (buoy, altimeter), ensures that the database can confidently be used for estimate extreme return waves. This can also have added benefits, as the survivability of the WECs will not be over-estimated, hence reducing the potential Capital Expenditure required.

## 6. Conclusions

In this study, the ECHOWAVE high-resolution wave dataset for the North-East Atlantic, was presented and validated. The hindcast was created using a multi-grid implementation of the WAVEWATCH III model with a maximum spatial resolution of 0.03° along European coasts. The main aim of this dataset is to be used in the context of wave resource assessments in the area, and as input for the simulation of wave energy converters' (WEC) operation. To this point, the hindcast covers 30 years, from 1992 to 2021.

We have revisited the parameterizations' adjustments proposed by Alday et al. [11] which lead to T475. Further adjustments were applied to the wind input and swell dissipation terms to improve the model accuracy in the North-East Atlantic. The final set of parameters' values, defined as TUD-165, was obtained through sensitivity analysis comparing the simulated wave heights with altimeter data from the Sea State CCI V3 product. The effects of the adjustments leading to TUD-165, were first analyzed at basin scale only using altimeter data and then verified with buoy data (in deep and intermediate waters).

Results using TUD-165 showed (in average) a 2.5% reduction of the $H_s$ positive bias for wave heights < 6 m at basin scale, compared to T475. No significant changes were observed in the SI or HH index. When comparing with Jason-2 from CCI V3, TUD-165 helped to reduce the underestimation of occurrences of $H_s$ in the range of 1 to 1.5 m. This comes with a small increase in the occurrences at 2 m.

Extensive validation of the model was done within the European coastal shelf. The use of the complete time periods available for 5 altimeters (Jason-1, Jason-2, Jason-3, Envisat and Saral) helped to provide a well defined variability range of the wave heights performance parameters. In average the NMB in the neighborhood of the most frequent $H_s$ (2 m) is 3%, an smaller for larger wave heights. The $H_s$ scatter index and HH index are typically < 10% for wave heights > 2 m. Results also show that the wind correction values applied to the ERA5 forcing, is effective to reduce the otherwise strong underestimation of larger $H_s$ with maximum NMB of only -4%. In general it was verified that the $H_s$ bias levels and wave height distribution from ECHOWAVE are similar than those of the WAVERYS reanalysis within the North-East Atlantic for wave heights < 9.5 m. For larger wave heights, ECHOWAVE shows better skills.

Analysis of spectral energy mean distribution suggests that, the model performs better during stronger wind conditions, capturing storm waves that are valuable for survivability estimations of WECs. Further validation with over 30 buoys (year 2020), using wave parameters like $H_s$, $T_p$ and $T_{02}$, points to a good performance of the implemented model across the domain. In general NMB for $H_s$ are $\leq 5\%$ and $\leq 10\%$ for $T_{02}$, with high correlation levels typically $> 0.95$ for $H_s$ and $> 0.9$ for $T_{02}$. Although not shown in this study, similar results were computed for 2021, 2014 and 2010.

One of the main advantages of ECHOWAVE is that it provides high spatial (∼ 2.3 km) and temporal (1 hr) resolution data for depths $< 200$ m covering most of the areas of interest for wave energy projects within the EU and the UK. This allows a more accurate estimation of the wave energy flux compared to existing global datasets (like ERA5 or WAVERYS) that can lead to an underestimation of pWave $\geq -25\%$ in coastal zones.

Recent efforts have been made to incorporate the Gaussian Quadratures Method (GQM; [46]) in WW3. This has made it affordable to compute the full nonlinear wave interactions with lower CPU usage than, for example, the WRT method as implemented by van Vledder [50]. at this stage, the GQM has been implemented for open ocean (deep water) applications only. It was shown in [47] that the use of GQM together with the highly directional wave breaking parameterization proposed by Romero [79] is of great benefit for the representation of realistic spectral shapes at high frequencies. It is expected that this approach, plus further parameterization adjustments, will be beneficial for the simulation of more accurate spectral energy levels in general. As a result, this would help to obtain better estimations of WEC responses, reducing the uncertainties in the computations of produced power. This analysis will be included in a follow-up study.

## CRediT authorship contribution statement

**Matías Alday:** Writing – review & editing, Writing – original draft, Validation, Software, Methodology, Investigation, Formal analysis, Data curation, Conceptualization. **George Lavidas:** Writing – review & editing, Resources, Project administration, Investigation, Funding acquisition, Data curation.

## Declaration of competing interest

The authors declare that they have no known competing financial interests or personal relationships that could have appeared to influence the work reported in this paper.

## Data availability

The Marine Renewable Energies Lab (MREL) promotes and favor use of the ECHOWAVE dataset for research purposes, under CC BY-NC-SA with proper attribution. For all enquiries on the ECHOWAVE dataset (wave parameters' fields and spectral files), please contact George Lavidas: g.lavidas@tudelft.nl, and Matias Alday Gonzalez: M.F.aldaygonzalez@tudelft.nl. Additionally, a data request link will be added on the MREL website (under the tab Datasets & Models) https://www.tudelft.nl/ceg/mrel.

## Acknowledgments

The authors acknowledge the use of computational resources of DelftBlue supercomputer, provided by Delft High Performance Computing Centre (https://www.tudelft.nl/dhpc). Special thanks to Dennis Palagin who helped with the WW3 compiling scripts in DelftBlue and to Mickael Accensi who provided the scripts to read and compare altimeter data with WW3 output. Many thanks to the anonymous reviewers who thoroughly read the study, pointing out details, and provided valuable feedback to improve the manuscript. This work is part of the EU-SCORES project that has received funding from the European Union's Horizon 2020 research and innovation programme under grant agreement No 101036457 (https://euscores.eu).

## Appendix A. Model implementation details

All simulations were performed using WAVEWATCH III version 7.14. The following switches for physical parameterizations and numerical choices were included in the model compilation:

- NOGRB SCRIP SCRIPNC TRKNC DIST MPI PR3 UQ FLX0 LN1 ST4 STAB0 NL1 BT4 DB1 MLIM TR0 BS0 IC2 IS2 REF1 IG1 WNT2 WNX1 RWND WCOR CRT1 CRX1 TIDE O0 O1 O2 O2a O2b O2c O3 O4 O5 O6 O7

The following parameters' values were included in the namelist from the TUD-165 parameterization used in the ECHOWAVE hindcast:

- Wave growth and swell dissipation in SIN4 namelist: BETAMAX = 1.65, SWELLF = 0.68, TAUWSHELTER = 0.3, SWELLF3 = 0.022, SWELLF4 = 90000.0, SWELLF7 = 360000.0
- Wave reflection parameters in namelist REF1: REFCOAST = 0.05, REFCOSP_STRAIGHT = 4, REFFREQ = 1., REFICEBERG = 0.2, REFMAP = 0., REFSLOPE = 2., REFSUBGRID = 0.1, REFRMAX = 0.5
- MISC namelist including wind correction terms: ICEHINIT = 0.8, ICEHMIN = 0.1, CICE0 = 0.25, NOSW = 6, CICEN = 2.00, LICE = 40 000., FLAGTR = 4, FACBERG = 0.2, WCOR1 = 20.5,WCOR2 = 1.04

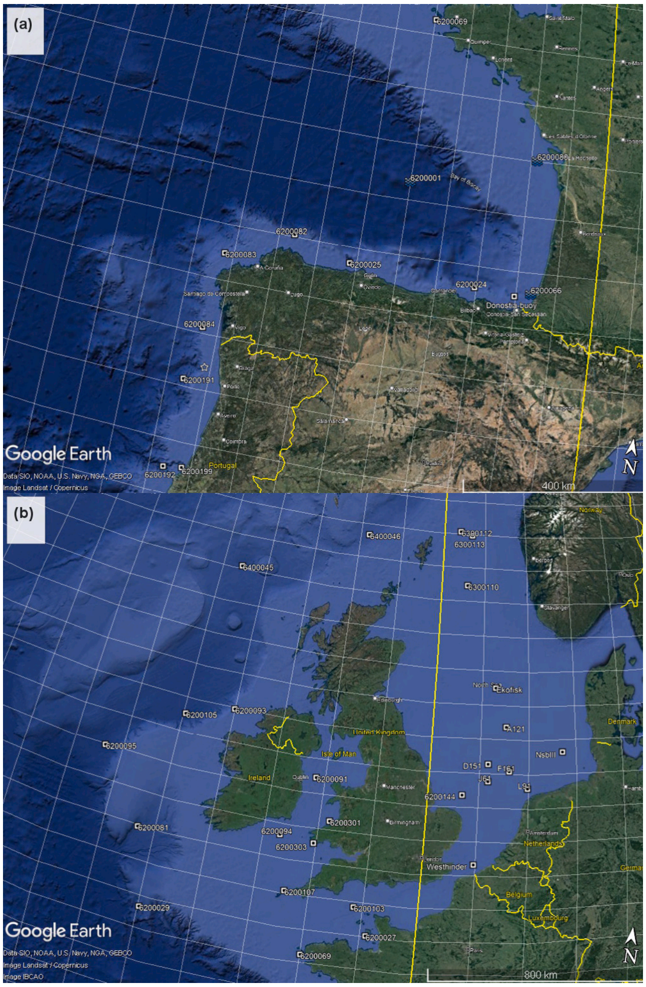

**Fig. B.14.** Buoys location map: (a) Bay of Biscay, (b) North Sea, English Channel and the UK. Map data from ©Google Landast/Copernicus.

## Appendix B. Buoys locations

Locations of all buoys used in the validation of the dataset are included in Fig. B.14.

## References

[1] N. Guillou, G. Lavidas, G. Chapalain, Wave energy resource assessment for exploitation—a review, J. Mar. Sci. Eng. 8 (9) (2020) 705, http://dx.doi.org/10.3390/jmse8090705.

[2] K. Gunn, C. Stock-Williams, Quantifying the global wave power resource, Renew. Energy 44 (2012) 296–304, http://dx.doi.org/10.1016/j.renene.2012.01.101.

[3] N. Li, G. García-Medina, K.F. Cheung, Z. Yang, Wave energy resources assessment for the multi-modal sea state of Hawaii, Renew. Energy 174 (2021) 1036–1055.

[4] A. Ribal, A.V. Babanin, S. Zieger, Q. Liu, A high-resolution wave energy resource assessment of Indonesia, Renew. Energy 160 (2020) 1349–1363, http://dx.doi.org/10.1016/j.renene.2020.06.017.

[5] G. Lavidas, V. Venugopal, Application of numerical wave models at European coastlines : A review, Renew. Sustain. Energy Rev. 92 (2018) 489–500, http://dx.doi.org/10.1016/j.rser.2018.04.112.

[6] F. Lucero, P.A. Catalán, Á. Ossandón, J. Beyá, A. Puelma, L. Zamorano, Wave energy assessment in the central-south coast of Chile, Renew. Energy 114 (2017) 120–131.

[7] G. Besio, L. Mentaschi, A. Mazzino, Wave energy resource assessment in the mediterranean sea on the basis of a 35-year hindcast, Energy 94 (2016) 50–63.

[8] J.C. van Nieuwkoop, H.C. Smith, G.H. Smith, L. Johanning, Wave resource assessment along the cornish coast (UK) from a 23-year hindcast dataset validated against buoy measurements, Renew. Energy 58 (2013) 1–14, http://dx.doi.org/10.1016/j.renene.2013.02.033.

[9] European Commission, An EU strategy to harness the potential of offshore renewable energy for a climate neutral future, 2020, URL: https://eur-lex.europa.eu/legal-content/EN/TXT/PDF/?uri=CELEX:52020DC0741.

[10] M. Accensi, M. Alday, C. Maisondieu, N. Raillard, D. Darbynian, C. Old, B. Sellar, O. Thilleul, Y. Perignon, G. Payne, L. O'Boyle, L. Fernandez, F. Dias, R. Chumbinho, G. Guitton, ResourceCODE framework: A high-resolution wave parameter dataset for the European shelf and analysis toolbox, 2021, URL: https://archimer.ifremer.fr/doc/00736/84812/.

[11] M. Alday, M. Accensi, F. Ardhuin, G. Dodet, A global wave parameter database for geophysical applications. Part 3: Improved forcing and spectral resolution, Ocean Model. 166 (2021) 101848, http://dx.doi.org/10.1016/j.ocemod.2021.101848.

[12] G. Korres, M. Ravdas, A. Zacharioudaki, D. Denaxa, M. Sotiropoulou, Mediterranean sea waves reanalysis (CMEMS med-waves, MedWAM3 system)(version 1) set. Copernicus monitoring environment marine service (CMEMS), 2021.

[13] H. Hersbach, B. Bell, P. Berrisford, S. Hirahara, A. Horányi, J. Muñoz-Sabater, J. Nicolas, C. Peubey, R. Radu, D. Schepers, et al., The ERA5 global reanalysis, Q. J. R. Meteorol. Soc. 146 (730) (2020) 1999–2049, http://dx.doi.org/10.1002/qj.3803.

[14] G. Lavidas, H. Polinder, North sea wave database (NSWD) and the need for reliable resource data: A 38 year database for metocean and wave energy assessments, Atmosphere 10 (9) (2019) 551.

[15] J. Perez, M. Menendez, I.J. Losada, GOW2: A global wave hindcast for coastal applications, Coast. Eng. 124 (2017) 1–11, http://dx.doi.org/10.1016/j.coastaleng.2017.03.005.

[16] N. Rascle, F. Ardhuin, A global wave parameter database for geophysical applications. Part 2: model validation with improved source term parameterization, Ocean Model. 70 (2013) 174–188, http://dx.doi.org/10.1016/j.ocemod.2012.12.001.

[17] A. Chawla, D.M. Spindler, H.L. Tolman, Validation of a thirty year wave hindcast using the climate forecast system reanalysis winds, Ocean Model. 70 (2013) 189–206.

[18] S. Law-Chune, L. Aouf, A. Dalphinet, B. Levier, Y. Drillet, M. Drevillon, WAVERYS: a CMEMS global wave reanalysis during the altimetry period, Ocean Dyn. 71 (2021) 357–378, http://dx.doi.org/10.1007/s10236-020-01433-w.

[19] T. Kodaira, K. Sasmal, R. Miratsu, T. Fukui, T. Zhu, T. Waseda, Uncertainty in wave hindcasts in the north atlantic ocean, Mar. Struct. 89 (2023) 103370.

[20] J.E. Stopa, K.F. Cheung, Intercomparison of wind and wave data from the ECMWF reanalysis interim and the NCEP climate forecast system reanalysis, Ocean Model. 75 (2014) 65–83, http://dx.doi.org/10.1016/j.ocemod.2013.12.006.

[21] J.E. Stopa, F. Ardhuin, E. Stutzmann, T. Lecocq, Sea state trends and variability: consistency between models, altimeters, buoys, and seismic data (1979–2016), J. Geophys. Res.: Oceans 124 (6) (2019) 3923–3940, http://dx.doi.org/10.1029/2018JC014607.

[22] E.B. Mackay, A.S. Bahaj, P.G. Challenor, Uncertainty in wave energy resource assessment. Part 1: Historic data, Renew. Energy 35 (8) (2010) 1792–1808.

[23] WAMDI Group, The WAM model - a third generation ocean wave prediction model, J. Phys. Oceanogr. 18 (1988) 1775–1810, URL: http://journals.ametsoc.org/doi/pdf/10.1175/1520-0485%281988%29018%3C1775%3ATWMTGO%3E2.0.CO%3B2.

[24] The WAVEWATCH III® Development Group, User Manual and System Documentation of WAVEWATCH III® Version 6.07, Tech. Note 333, NOAA/NWS/NCEP/MMAB, College Park, MD, USA, 2019, 465 pp. + Appendices.

[25] H.L. Tolman, The Numerical Model WAVEWATCH: A Third Generation Model for Hindcasting of Wind Waves on Tides in Shelf Seas, Technical Report 89–2, Faculty of civil engineering, Delft University of Technology, 1989, ISSN 0169-6548.

[26] M. Alday, F. Ardhuin, G. Dodet, M. Accensi, Accuracy of numerical wave model results: application to the atlantic coasts of Europe, Ocean Sci. 18 (6) (2022) 1665–1689, http://dx.doi.org/10.5194/os-18-1665-2022.

[27] A. Chawla, H.L. Tolman, V. Gerald, D. Spindler, T. Spindler, J.-H.G.M. Alves, D. Cao, J.L. Hanson, E.-M. Devaliere, A multigrid wave forecasting model: A new paradigm in operational wave forecasting, Weather Forecast. 28 (2013) 1057–1078, http://dx.doi.org/10.1175/waf-d-12-00007.1.

[28] J.-F. Piollé, G. Dodet, Y. Quilfen, M. Schwatke, G. Quartly, P. Thibaut, ESA Sea State Climate Change Initiative (Sea_State_cci): Global Remote Sensing Multi-Mission Along-Track Significant Wave Height From Altimetry, L2P Product, Version 3, NERC EDS Centre for Environmental Data Analysis, 2022, http://dx.doi.org/10.5285/8cb46a5efaa74032bf1833438f499cc3.

[29] M. Passaro, M.A. Hemer, G.D. Quartly, C. Schwatke, D. Dettmering, F. Seitz, Global coastal attenuation of wind-waves observed with radar altimetry, Nature Commun. 12 (1) (2021) 3812.

[30] F. Schlembach, M. Passaro, G.D. Quartly, A. Kurekin, F. Nencioli, G. Dodet, J.-F. Piollé, F. Ardhuin, J. Bidlot, C. Schwatke, et al., Round robin assessment of radar altimeter low resolution mode and delay-Doppler retracking algorithms for significant wave height, Remote Sens. 12 (8) (2020) 1254, http://dx.doi.org/10.3390/rs12081254.

[31] G. Lavidas, V. Venugopal, D. Friedrich, Wave energy extraction in Scotland through an improved nearshore wave atlas, Int. J. Mar. Energy 17 (2017) 64–83.

[32] J.-M. Lellouche, E. Greiner, O. Le Galloudec, G. Garric, C. Regnier, M. Drevillon, M. Benkiran, C.-E. Testut, R. Bourdalle-Badie, F. Gasparin, et al., Recent updates to the copernicus marine service global ocean monitoring and forecasting real-time 1/12° high-resolution system, Ocean Sci. 14 (5) (2018) 1093–1126.

[33] W.H.F. Smith, R. Scharroo, Waveform aliasing in satellite radar altimetry, IEEE Trans. Geosci. Remote Sens. 53 (2015) 1671–1682, http://dx.doi.org/10.1109/TGRS.2014.2331193.

[34] L. Mentaschi, G. Besio, F. Cassola, A. Mazzino, Performance evaluation of wavewatch III in the Mediterranean sea, Ocean Model. 90 (2015) 82–94, http://dx.doi.org/10.1016/j.ocemod.2015.04.003.

[35] R.G. Dean, R.A. Dalrymple, Water Wave Mechanics for Engineers and Scientists, second ed., World Scientific, Singapore, 1991, p. 353.

[36] G.B. Airy, Tides and waves, in: H.J. Rose, et al. (Eds.), Encyclopedia Metropolitana (1817–1845), London, 1841.

[37] H.L. Tolman, A mosaic approach to wind wave modeling, Ocean Model. 25 (2008) 35–47, http://dx.doi.org/10.1016/j.ocemod.2008.06.005.

[38] M.F. Alday, V. Raghavan, G. Lavidas, Analysis of the north atlantic offshore energy flux from different reanalysis and hindcasts, in: Vol. 15 (2023): Proceedings of the European Wave and Tidal Energy Conference, Vol. 15, EWTEC, 2023, http://dx.doi.org/10.36688/ewtec-2023-140.

[39] F. Ardhuin, E. Rogers, A. Babanin, J.-F. Filipot, R. Magne, A. Roland, A. van der Westhuysen, P. Queffeulou, J.-M. Lefevre, L. Aouf, F. Collard, Semi-empirical dissipation source functions for wind-wave models: part i, definition, calibration and validation, J. Phys. Oceanogr. 40 (9) (2010) 1917–1941, http://dx.doi.org/10.1175/2010JPO4324.1.

[40] P.A.E.M. Janssen, Quasi-linear theory of wind wave generation applied to wave forecasting, J. Phys. Oceanogr. 21 (1991) 1631–1642, URL: http://dx.doi.org/10.1175/1520-0485(1991)021%3C1631:QLTOWW%3E2.0.CO;2. See comments by D. Chalikov, J. Phys. Oceanogr. 1993, vol. 23 pp. 1597–1600.

[41] J. Bidlot, P.A.E.M. Janssen, S. Abdalla, A Revised Formulation for Ocean Wave Dissipation in CY25R1, Technical Report Memorandum R60.9/JB/0516, Research Department, ECMWF, Reading, U. K., 2005, p. 35.

[42] J. Bidlot, P.A.E.M. Janssen, S. Abdalla, A Revised Formulation of Ocean Wave Dissipation and Its Model Impact, Technical Report 509, ECMWF, Reading, U. K., 2007, p. 27.

[43] F. Ardhuin, B. Chapron, F. Collard, Observation of swell dissipation across oceans, Geophys. Res. Lett. 36 (2009) L06607, http://dx.doi.org/10.1029/2008GL037030.

[44] F. Leckler, Observation et Modélisation du Déferlement des Vagues (Ph.D. thesis), Université Européenne de Bretagne, Ecole doctorale des Sciences de la Mer, Brest, France, 2013, p. 240, URL: http://tinyurl.com/leckler-thesis.

[45] S. Hasselmann, K. Hasselmann, Computation and parameterizations of the nonlinear energy transfer in a gravity-wave spectrum. Part I: a new method for efficient computations of the exact nonlinear transfer, J. Phys. Oceanogr. 15 (1985) 1369–1377, http://dx.doi.org/10.1175/1520-0485(1985)015<1369:CAPOTN>2.0.CO;2.

[46] I.V. Lavrenov, Effect of wind wave parameter fluctuation on the nonlinear spectrum evolution, J. Phys. Oceanogr. 31 (2001) 861–873, URL: http://ams.allenpress.com/archive/1520-0485/31/4/pdf/i1520-0485-31-4-861.

[47] M. Alday, F. Ardhuin, On consistent parameterizations for both dominant wind-waves and spectral tail directionality, J. Geophys. Res.: Oceans (2023) e2022JC019581, http://dx.doi.org/10.1029/2022JC019581.

[48] D.J. Webb, Non-linear transfer between sea waves, Deep Sea Res. 25 (1978) 279–298, http://dx.doi.org/10.1016/0146-6291(78)90593-3.

[49] B.A. Tracy, D.T. Resio, Theory and Calculation of the Nonlinear Energy Transfer Between Sea Waves in Deep Water, Technical Report 11, U.S. Army Engineer Waterways Experiment Station, Vicksburg, U.S.A., 1982.

[50] G.P. van Vledder, The WRT method for the computation of non-linear four-wave interactions in discrete spectral wave models, Coast. Eng. 53 (2–3) (2006) 223–242.

[51] G. Boutin, F. Ardhuin, D. Dumont, C. Sévigny, F. Girard-Ardhuin, Floe size effects on wave-ice interactions: theoretical background, implementation and applications, J. Geophys. Res. 123 (2018) 4779–4805, http://dx.doi.org/10.1029/2017JC013622.

[52] F. Ardhuin, M. Otero, S. Merrifield, A. Grouazel, E. Terrill, Ice breakup controls dissipation of wind waves across southern ocean sea ice, Geophys. Res. Lett. 47 (2020) e2020GL087699, http://dx.doi.org/10.1029/2020GL087699.

[53] J.E. Stopa, F. Ardhuin, F. Girard-Ardhuin, Wave climate in the arctic 1992–2014: seasonality and trends, Cryosphere 10 (2016) 1605–1629, http://dx.doi.org/10.5194/tc-10-1605-2016.

[54] F. Ardhuin, W.C. O'Reilly, T.H.C. Herbers, P.F. Jessen, Swell transformation across the continental shelf. Part I: Attenuation and directional broadening, J. Phys. Oceanogr. 33 (2003) 1921–1939, URL: http://journals.ametsoc.org/doi/pdf/10.1175/1520-0485%282003%29033%3C1921%3ASTATCS%3E2.0.CO%3B2.

[55] H.L. Tolman, Subgrid modeling of moveable-bed bottom friction in wind wave models, Coast. Eng. 26 (1995) 57–75, http://dx.doi.org/10.1016/0378-3839(95)00016-0.

[56] F. Ardhuin, A. Roland, Coastal wave reflection, directional spreading, and seismo-acoustic noise sources, J. Geophys. Res. 117 (2012) C00J20, http://dx.doi.org/10.1029/2011JC007832.

[57] B.P. Leonard, The ULTIMATE conservative difference scheme applied to unsteady one-dimensional advection, Comput. Methods Appl. Mech. Eng. 88 (1991) 17–74.

[58] R. Davis, E. Moore, A numerical study of vortex shedding from rectangles, J. Fluid Mech. 116 (1982) 475–506, http://dx.doi.org/10.1017/S0022112082000561.

[59] H.L. Tolman, Alleviating the garden sprinkler effect in wind wave models, Ocean Model. 4 (2002) 269–289, http://dx.doi.org/10.1016/S1463-5003(02)00004-5.

[60] Y. Perignon, F. Ardhuin, M. Cathelain, M. Robert, Swell dissipation by induced atmospheric shear stress, J. Geophys. Res. 119 (2014) 6622–6630, http://dx.doi.org/10.1002/2014JC009896.

[61] W.D. Grant, O.S. Madsen, Combined wave and current interaction with a rough bottom, J. Geophys. Res. 84 (1979) 1797–1808, http://dx.doi.org/10.1029/JC084iC04p01797.

[62] F. Girard-Ardhuin, R. Ezraty, Enhanced arctic sea ice drift estimation merging radiometer and scatterometer data, IEEE Trans. Geosci. Remote Sens. 50 (2012) 2639–2648, http://dx.doi.org/10.1109/TGRS.2012.2184124.

[63] F. Ardhuin, F. Dumas, A.-C. Bennis, A. Roland, A. Sentchev, P. Forget, J. Wolf, F. Girard, P. Osuna, M. Benoit, Numerical wave modeling in conditions with strong currents: dissipation, refraction and relative wind, J. Phys. Oceanogr. 42 (2012) 2101–2120, http://dx.doi.org/10.1175/JPO-D-11-0220.1.

[64] E.R. Echevarria, M.A. Hemer, N.J. Holbrook, Global implications of surface current modulation of the wind-wave field, Ocean Model. 161 (2021) 101792.

[65] G. Marechal, F. Ardhuin, Surface currents and significant wave height gradients: Matching numerical models and high-resolution altimeter wave heights in the agulhas current region, J. Geophys. Res.: Oceans 126 (2) (2021) e2020JC016564, http://dx.doi.org/10.1029/2020JC016564.

[66] M.-H. Rio, S. Mulet, N. Picot, Beyond GOCE for the ocean circulation estimate: Synergetic use of altimetry, gravimetry, and in situ data provides new insight into geostrophic and Ekman currents, Geophys. Res. Lett. 41 (2014) 8918–8925, http://dx.doi.org/10.1002/2014GL061773.

[67] S. Mulet, M.-H. Rio, H. Etienne, C. Artana, M. Cancet, G. Dibarboure, H. Feng, R. Husson, N. Picot, C. Provost, et al., The new CNES-CLS18 global mean dynamic topography, Ocean Sci. Discuss. (2021) 1–31.

[68] J.-F. Filipot, F. Ardhuin, A unified spectral parameterization for wave breaking: From the deep ocean to the surf zone, J. Geophys. Res.: Oceans 117 (C11) (2012) http://dx.doi.org/10.1029/2011JC007784.

[69] GEBCO Compilation Group, GEBCO_2021 grid (accessed on 8 june 2021), 2021, URL: https://doi.org/10.5285/c6612cbe-50b3-0cff-e053-6c86abc09f8f.

[70] G. Dodet, J.-F. Piolle, Y. Quilfen, S. Abdalla, M. Accensi, F. Ardhuin, E. Ash, J.-R. Bidlot, C. Gommenginger, G. Marechal, M. Passaro, G. Quartly, J. Stopa, B. Timmermans, I. Young, P. Cipollini, C. Donlon, The sea state CCI dataset v1: towards a sea state climate data record based on satellite observations, Earth Syst. Sci. Data 12 (2020) 1929–1951, http://dx.doi.org/10.5194/essd-12-1929-2020.

[71] J. Hanafin, Y. Quilfen, F. Ardhuin, J. Sienkiewicz, P. Queffeulou, M. Obrebski, B. Chapron, N. Reul, F. Collard, D. Corman, E.B. de Azevedo, D. Vandemark, E. Stutzmann, Phenomenal sea states and swell radiation: a comprehensive analysis of the 12-16 February 2011 North Atlantic storms, Bull. Am. Meteorol. Soc. 93 (2012) 1825–1832, http://dx.doi.org/10.1175/BAMS-D-11-00128.1.

[72] M. Passaro, P. Cipollini, S. Vignudelli, G.D. Quartly, H.M. Snaith, ALES: A multi-mission adaptive subwaveform retracker for coastal and open ocean altimetry, Remote Sens. Environ. 145 (2014) 173–189, http://dx.doi.org/10.1016/j.rse.2014.02.008.

[73] F. Peng, X. Deng, A new retracking technique for brown peaky altimetric waveforms, Mar. Geod. 41 (2) (2018) 99–125, http://dx.doi.org/10.1080/01490419.2017.1381656.

[74] G. Dibarboure, A. Lamy, M.-I. Pujol, G. Jettou, The drifting phase of SARAL: Securing stable ocean mesoscale sampling with an unmaintained decaying altitude, Remote Sens. 10 (7) (2018) 1051, http://dx.doi.org/10.3390/rs10071051.

[75] D. Krishna, K. Vikram, K. Sreejith, SARAL/AltiKa measurements for geodetic applications: Impact of drifting and mispointing phase data, Adv. Space Res. 72 (9) (2023) 4021–4030, http://dx.doi.org/10.1016/j.asr.2023.07.032.

[76] A. Roland, F. Ardhuin, On the developments of spectral wave models: numerics and parameterizations for the coastal ocean, Ocean Dyn. 64 (6) (2014) 833–846, http://dx.doi.org/10.1007/s10236-014-0711-z.

[77] M.A. Chatzigiannakou, L. Ulvgård, I. Temiz, M. Leijon, Offshore deployments of wave energy converters by uppsala university, Sweden, Mar. Syst. Ocean Technol. 14 (2019) 67–74, http://dx.doi.org/10.1007/s40868-019-00055-2.

[78] T.H. Durrant, D.J. Greenslade, I. Simmonds, Validation of Jason-1 and envisat remotely sensed wave heights, J. Atmos. Ocean. Technol. 26 (1) (2009) 123–134, http://dx.doi.org/10.1175/2008JTECHO598.1.

[79] L. Romero, Distribution of surface wave breaking fronts, Geophys. Res. Lett. 46 (2019) 10463–10474, http://dx.doi.org/10.1029/2019GL083408.